The Astrophysical Journal, 816:40 (19pp), 2016 January 1 doi:10.3847/0004-637X/816/1/40

RESOLVING IONIZATION AND METALLICITY ON PARSEC SCALES ACROSS MRK 71 WITH *HST*-WFC3

Bethan L. James[1], Matthew Auger[1], Alessandra Aloisi[2], Daniela Calzetti[3], and Lisa Kewley[4,5]
[1] Institute of Astronomy, University of Cambridge, Madingley Road, Cambridge, CB3 0HA, UK; bjames@ast.cam.ac.uk
[2] Space Telescope Science Institute, 3700 San Martin Drive, Baltimore, MD 21218, USA
[3] Department of Astronomy, University of Massachusetts, Amherst, MA 01003, USA
[4] RSAA, Australian National University, Cotter Road, Weston Creek, ACT 2611, Australia
[5] Institute for Astronomy, 2680 Woodlawn Drive, University of Hawaii, Hilo, HI 96822, USA
Received 2015 September 9; accepted 2015 November 7; published 2015 December 30

ABSTRACT

Blue compact dwarf (BCD) galaxies in the nearby universe provide a means for studying feedback mechanisms and star formation processes in low-metallicity environments in great detail. Owing to their vicinity, these local analogs to primordial young galaxies are well suited for high-resolution studies that are unfeasible for high-redshift galaxies. Here we present *Hubble Space Telescope* Wide Field Camera 3 observations of one such BCD, Mrk 71, one of the most powerful local starbursts known, in the light of [O II], He II, Hβ, [O III], Hα, and [S II]. At $D \simeq 3.44$ Mpc, this extensive suite of emission-line images enables us to explore the chemical and physical conditions of Mrk 71 on $\sim$2 pc scales. We use emission-line diagnostics to distinguish ionization mechanisms on a pixel-by-pixel basis and show that despite the previously reported hypersonic gas and superbubble blowout, the gas in Mrk 71 is photoionized, with no sign of shock-excited emission. He II emission line images are used to identify up to six Wolf-Rayet stars, three of which lie on the edge of a blowout region. Using strong-line metallicity diagnostics, we present the first "metallicity image" of a galaxy, revealing chemical inhomogeneity on scales of $<$50 pc. We additionally demonstrate that while chemical structure can be lost at large scales, metallicity diagnostics can break down on spatial scales smaller than an H II region. This study highlights not only the benefits of high-resolution spatially resolved observations in assessing the effects of feedback mechanisms but also the potential limitations when employing emission-line diagnostics; these results are particularly relevant as we enter the era of extremely large telescopes.

Key words: galaxies: abundances – galaxies: individual (Mrk 71) – galaxies: star formation – stars: winds, outflows – stars: Wolf-Rayet – techniques: imaging spectroscopy

1. INTRODUCTION

Observations of blue compact dwarf (BCD) galaxies in the nearby universe provide a means for studying chemical evolution and star formation processes in chemically unevolved environments. BCDs are thought to have experienced only very low level star formation in the past, but are currently undergoing bursts of star formation in relatively pristine environments, ranging from $1/50$ to $1/2\,Z_{\odot}$ (Kunth & Östlin 2000), making them ideal analogs to young "building-block" galaxies in the high-z primordial universe (Searle & Sargent 1972).

One of the most powerful aspects of this analogous population is the fine spatial scales on which we can explore them compared to high-z galaxies—allowing us to gain insight into chemical and physical processes that occur on subkiloparsec scales within metal-poor environments. Spatially resolved observations of these systems are growing rapidly in both number and quality, owing to increasing IFU (integral field unit) capabilities (with seeing-limited spatial resolutions of $0\farcs2$) and the initiation of extensive volume-limited IFU surveys such as ATLAS 3D (Cappellari et al. 2011), SAMI (Bryant et al. 2015), and MANGA (Bundy et al. 2015). Moreover, with the addition of adaptive-optics systems, IFU observations are now able to probe emission lines on ultrafine spatial scales (e.g., $\sim$3 pc per spaxel at $\sim$4 Mpc; Müller Sánchez et al. 2006). As we enter the 30–40 m telescope era, such scales will also be reachable in the more distant universe, enabling us to resolve and explore structure in star-forming galaxies at the peak of cosmic star formation ($z = 2$–3). Until then, however, we continue to use high-resolution observations of their nearby counterparts, BCDs, to further our understanding of the intricacies of galaxy formation and evolution and prepare us for the types of structure that we will eventually probe at high z.

Much effort is already under way to understand the interstellar medium (ISM) of galaxies on $\lesssim$10 pc scales. Hydrodynamical simulations at high spatial resolutions (i.e., 1.5–12 pc) are being used to understand the triggering and evolution of star formation (e.g., Teyssier et al. 2010; Perret et al. 2014; Renaud et al. 2014). For example, by modeling a "realistic" ISM (i.e., inhomogeneous and thermally unstable), Teyssier et al. (2010) find that starbursts are not primarily due to large-scale inflows of gas, but rather gas fragmentation into massive and dense clouds. However, many questions concerning the details of ISM structure of star-forming galaxies still remain open.

First, we must understand the sources of ionization and the ionization processes within BCDs. At present BCDs are modeled as giant H II regions where photoionization is the dominant ionization mechanism influencing the ISM. However, the discovery of BCDs with significantly broad emission lines indicates that feedback mechanisms such as shocks, circumstellar emission, or even active galactic nuclei (AGNs) may also play a significant role (e.g., Izotov et al. 2007). Such feedback mechanisms are thought to have a strong influence on the evolution of dwarf galaxies (Marconi et al. 1994; Martin 1998; Ferrara & Tolstoy 2000; Calzetti et al. 2004), although exact details of the process are still uncertain and depend on the nature and geometry of the galaxy (De Young & Heckman 1994). The energy injected into the ISM by

supernova explosions can act as regulating mechanisms by heating and/or removing gas from the site of star formation (Kennicutt 1989; Heckman et al. 1997; Mac Low & Ferrara 1999) and quenching the star formation, whereas ionization and shock fronts through the ISM may cause star formation to propagate spatially (Elmegreen & Lada 1977; McCray & Kafatos 1987). Processes like these, which suppress star formation, have been suggested as solutions for the inefficiency of dwarf galaxies to form stars (Guo et al. 2010) and for the "missing satellites" problem, i.e., the discrepancy between observed and CDM-predicted numbers of dwarf galaxies (Klypin et al. 1999; Bovill & Ricotti 2009).

Second, the question of chemical homogeneity of star-forming galaxies is still under debate. Oxygen abundance maps of star-forming galaxies have shown them to be both chemically homogeneous (e.g., Kehrig et al. 2008, 2013; James et al. 2010; Pérez-Montero et al. 2011) and with structure (e.g., López-Sánchez et al. 2011; Monreal-Ibero et al. 2012; James et al. 2013a, 2013b; Sánchez Almeida et al. 2014), implying that feedback mechanisms can have a range of effects on chemical homogeneity, and also that a range of ISM mixing timescales exists within these galaxies on small spatial scales. Such properties of H II regions and starburst galaxies have been a controversial topic for many decades (Kobulnicky & Skillman 1996, 1997; Kennicutt & Skillman 2001) and are essential in constraining chemical evolution models.

Third, the effects of stellar feedback in low-metallicity environments are yet to be constrained in detail. O stars within BCDs can reach 10^2–10^5 in number (Guseva et al. 2000). Such a population has a profound influence on the dynamics of the gas, with stellar winds and supernovae giving rise to outflows, superbubbles, and shocks. In such low-metallicity environments, fast shocks combined with dense ISM have been theorized to explain the narrow high-ionization emission lines (e.g., He II, [Fe V]) seen in the spectra of several BCDs with broad-component emission (Thuan & Izotov 2005). However, high densities are largely uncommon in BCDs, where densities typical of H II regions ($\sim$100 cm^{-3}) are usually detected. Wolf-Rayet (WR) stars (known to exist in more than 200 BCDs) can also produce characteristic broad emission in specific ions or "WR features" (e.g., He II λ4686) that originate in the envelopes of massive stars undergoing rapid mass loss. Recent attempts to map galaxies in the light of He II λ4686 have identified and mapped the WR stellar population (e.g., James et al. 2009; Kehrig et al. 2013, 2015; Westmoquette et al. 2013), although we are yet to assess its role by spatially correlating the WR features to the shock and feedback morphologies on fine spatial scales.

The most robust way to investigate these processes in BCDs is to spatially resolve their emission lines and subsequent chemical and physical properties and to connect these to the resolved stellar populations. This can be achieved in high spatial resolution with the use of *Hubble Space Telescope* (*HST*) narrowband imaging. Previous work (e.g., Calzetti et al. 1999, 2004; Hong et al. 2011) has shown that this method is highly efficient in investigating nonradiative ionization processes in local star-forming galaxies. The angular resolution of *HST* is crucial here, since shocks (one of the primary non-photoionized mechanisms expected) tend to create very thin (<10 pc) and filamentary fronts, which cannot currently be detected with ground-based images, spectra, or spatially resolved spectroscopy, as they become washed out by the "ocean" of photoionized gas emission (e.g., Calzetti et al. 2004). For example, the Wide Field Camera 3 (WFC3)/UVIS pixel size of 0.″04 implies that structure down to $\sim$1 pc can be resolved within nearby ($D \leqslant 5$ Mpc) BCDs, allowing one to trace the morphology of non-photoionized gas in unprecedented detail at spatial scales where we can disentangle a number of sources (e.g., H II regions, WR stars, shocks).

This paper aims to explore chemical homogeneity and understand the ionization mechanisms responsible for emission within a nearby BCD, Mrk 71 ($D \simeq 3.44$ Mpc)[6], and thereby assess the effect of feedback mechanisms on the energetics, structure, and star formation using *HST* narrowband imaging. Mrk 71 is an excellent case study for this, as spectroscopic observations of this galaxy show evidence for both a significant mechanical feedback component and signs of a WR population. The structure of the paper is as follows: Mrk 71 is described in detail in Section 2, followed by a description of our observations and data processing in Section 3. We discuss the final images in Section 4, along with information derived from the images, i.e., emission-line diagnostics, photoionization modeling, and metallicity and He II imaging. In Section 5 we discuss the benefits and limitations of ultrahigh spatial resolution observations. We conclude in Section 6.

2. MRK 71—A BRIEF OVERVIEW

Mrk 71 is one of the most powerful (local) starbursts known in the (local) universe and is famed for having the "best case of hypersonic gas" (Roy et al. 1991, 1992; Gonzalez-Delgado et al. 1994). Early optical spectroscopic observations by Kennicutt et al. (1980) revealed extremely high degrees of excitation, low amounts of reddening, and an unusually energetic source of ionization. Its faint, extended, and exceptionally broad (FWHM > 2300 km s^{-1}) emission lines were first reported by Roy et al. (1992), thought to be signatures of an expanding supershell. Owing to this extraordinary feature, this system has been observed from X-ray to far-infrared (FIR) wavelengths, with both imaging and spectroscopy. Here we provide a brief overview of these observations and studies from the literature.

Structurally, Mrk 71 is a large and massive chain of H II regions within the dwarf galaxy NGC 2366 (Kennicutt et al. 1980; Binette et al. 2009) and is classed as a cometary BCD. Following the nomenclature adopted by Drissen et al. (2000), the NGC 2366 complex comprises three regions, I–III, where NGC 2366-I forms Mrk 71 alone. Within Mrk 71 there are two main clusters, A and B. Each of these regions is labeled in Figure 1, where we present color-composite images created from new WFC3 narrow- and broadband images covering both NGC 2366-II and Mrk 71.

The nearby proximity of Mrk 71 ($D = 3.44$ Mpc) allows resolved stellar population studies. Using *HST*, Thuan & Izotov (2005) found the stellar population within Mrk 71 to consist of a young (<30 Myr) population of blue main-sequence stars, an intermediate population of blue and red supergiants (RSGs, 20–100 Myr), an old AGB star population >100 Myr, and red giant stars (>1 Gyr). These findings were consistent with Noeske et al. (2000), who estimated the age of the oldest stars in the low surface brightness component to be <3 Gyr.

[6] Here we adopt the Cepheid-derived distance by Tolstoy et al. (1995).

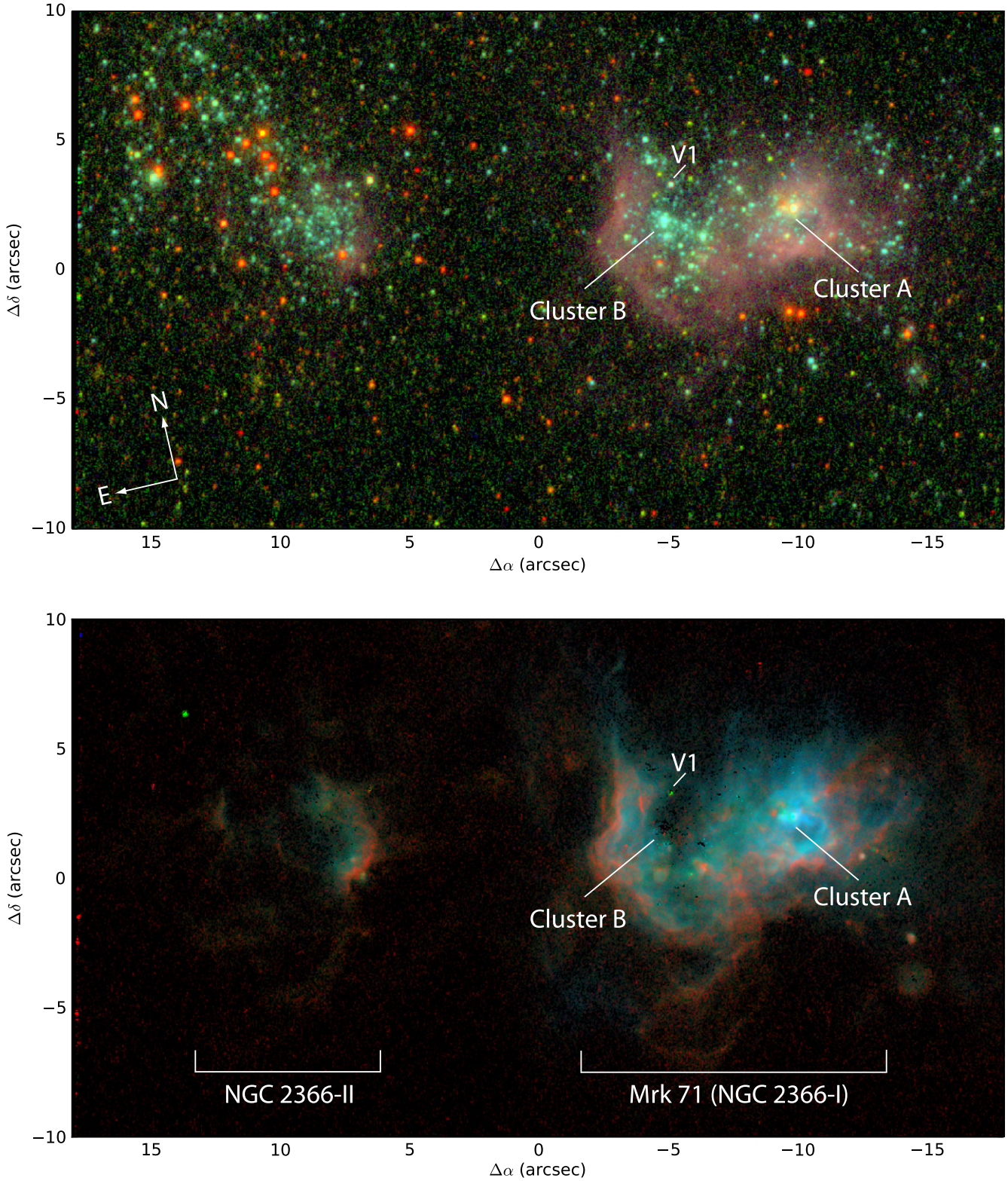

Figure 1. Color composites of Mrk 71 and NGC 2366-II with main clusters (A and B) and LBV star labeled (following the nomenclature of Drissen et al. 2000). Top panel: broadband images of stellar continuum—*I* band (red), *V* band (green), and *U* band (blue); bottom panel: narrowband, continuum-subtracted images of the ionized gas—F373N ([O II], red), F656N (Hα, green), and F502N ([O III], blue). The images have a spatial scale of $0\farcs04$ pixel^{-1} (0.67 pc pixel^{-1}) and are $36'' \times 20''$ in size (600 × 333 pc).

With regard to the individual stellar clusters, Drissen et al. (2000) report that both Mrk 71 and NGC 2366-II show RSGs. In Mrk 71 itself, cluster A is the younger (<1 Myr), more intense starburst with few visible stars, whereas cluster B is slightly older (3–4 Myr) and consists of many dozens of blue stars. Drissen et al. (2000) attribute an excess of He II λ4686 emission in cluster B to five WR stars, whereas no WR stars are detected in or around cluster A or NGC 2366-II. Additionally,

a rare luminous blue variable (LBV) is also present (labeled "V1"), which has been undergoing an eruption since 1994 (Drissen et al. 1997).

Chemically, long-slit optical observations show Mrk 71 to be metal-poor, with $\sim 1/6\ Z_{\odot}$[7] (Noeske et al. 2000; Thuan & Izotov 2005; Moustakas & Kennicutt 2006, i.e., $12 + \log(\mathrm{O/H}) = 7.89$). The oxygen abundances in several other H II regions along the body of Mrk 71 were found by Roy et al. (1996) to be slightly higher than the brightest region (cluster A).

The aforementioned broad emission line component of Mrk 71 was observed to extend from cluster A. Several mechanisms were put forward by Roy et al. (1992) to explain the emission, including stellar winds, Thomson scattering by hot electrons, supernova remnants, and a superbubble blowout (however, all were deemed unsatisfactory). This subject was revisited by Binette et al. (2009), who demonstrated that the emission could in fact be due to the interaction of high-velocity cluster winds with dense photoionized clumps. The super star cluster responsible for the intense nebular flux observed in cluster A shows no stellar UV absorption features (Drissen et al. 2000), suggesting that it is shrouded by dust. Furthermore, the optical–FIR spectral energy distribution (SED) of this cluster shows evidence that it is in an ultracompact H II region stage where newly formed stars are still embedded in their natal molecular clouds.

The broad emission of Mrk 71 made it an attractive candidate for hosting a low-metallicity AGN (Izotov et al. 2007). Follow-up X-ray observations by Thuan et al. (2014) detect four faint point sources coincident with a background AGN and a very compact H II region in cluster A, and two faint extended sources associated with massive H II complexes. However, no evidence for hard nonthermal radiation is seen in the optical spectrum of Mrk 71 (Izotov et al. 2007, and references therein).

Fabry–Perot observations by Roy et al. (1991) revealed emission-line splitting across a 240×307 pc region centered on cluster A (i.e., covering the entirety of Mrk 71), which was interpreted as a bubble expanding at a speed of $45\ \mathrm{km\ s^{-1}}$. Using population synthesis models, Drissen et al. (2000) show that the expanding bubble must be due to energy released by massive stars and supernova explosions throughout cluster B, rather than being blown by winds from massive stars within the core of the cluster. The same radial velocity maps of Roy et al. (1991) also uncovered a "chimney" structure extending away from the central bubble in the north–northwest direction, which aligns with the obvious cavity in emission seen extending north from cluster B in Figure 1 and the diffuse He II extended emission seen by Drissen et al. (2000).

Kinematically, [O III] and H I velocity maps of NGC 2366 (Roy et al. 1991; Braun 1995) suggest that NGC 2363 ($\sim$1.14 kpc NW of Mrk 71 and not covered here) may be disconnected from the main body of objects (Mrk 71 and NGC 2366-II, i.e., those under study here) and could in fact be a satellite galaxy that is interacting and perhaps triggering star formation in these objects. This is further supported by the fact that an age sequence is seen to exist along the main bodies: 10 Myr (NGC 2366-II), 3–5 Myr (Mrk 71-B), $<$1 Myr (Mrk 71-A).

[7] Throughout this paper we adopt the solar oxygen abundance of $12 + \log(\mathrm{O/H}) = 8.69$ from Asplund et al. (2009).

Table 1
Details of Observations Used within This Study

Filter	Emission line/band	T_{exp}/s
F336W	*U* band	300
F373N	[O II] λ3727+λ3729	900
F438W	*B* band	210
F469N	He II λ4686	5250
F487N	Hβ λ4861	1020
F502N	[O III] λ5007	540
F547M	*V* band	300
F656N	Hα λ6564	720
FQ672N	[S II] λ6716	2841
FQ674N	[S II] λ6732	2841
F814W	*I* band	420

Note. For each WFC3-UVIS filter we list the corresponding emission line or broadband emission observed within Mrk 71, along with the total exposure time used.

3. OBSERVATIONS AND DATA PROCESSING

The images used in this work are all obtained with the WFC3 UVIS channel on board *HST* and form part of observational program 13041 (PI: James), observed on 2013 March 6. A summary of the filters, the emission line or band covered by the filter, and the exposure times is given in Table 1. Since the focus of this work is on the ionized gas, as probed by strong emission lines, the emphasis will be on the narrowband filter observations. The observations in the medium- and broadband filters are primarily used for stellar continuum subtraction, as discussed in Section 3.1. Each narrowband filter was used to target a specific emission line within the optical spectrum of Mrk 71, which we show in Figure 2. The optical spectrum[8] was taken from Moustakas & Kennicutt (2006, hereafter MK06) and is described below in more detail.

The field of view (FOV) of each WFC3 broad- and narrowband observation subtends $2.7\ \mathrm{kpc^2}$ ($162'' \times 162''$), whereas quad-band filter observations subtend $0.45\ \mathrm{kpc^2}$ (i.e., 1/6 the WFC3 FOV after allowing for edge effects).

The WFC3/UVIS data set was processed through the CALWF3 pipeline version 1.0. The calibrated, flat-fielded individual exposures were corrected for charge transfer efficiency (CTE) losses by using a publicly available stand-alone program.[9] The resulting files were then aligned and combined using DRIZZLEPAC software. For each filter, individual exposures were aligned using TWEAKREG and combined using ASTRODRIZZLE. We then aligned the combined images across filters using the F336W image as the reference frame for the WCS. The final data products have a pixel scale of $4\ \mathrm{mas\ pixel^{-1}}$ and are in units of $\mathrm{e^-\ s^{-1}}$, which were converted to physical units using the WFC3 photometric zero points.

3.1. Continuum Subtraction

In order to create emission-line-only images, narrowband images were corrected for underlying stellar continua. The nebular emission lines contributing to the flux in each of the seven narrowband filters are listed in Table 1. Each narrowband filter targets a single major emission line (as illustrated in

[8] Available at http://www.sos.siena.edu/~jmoustakas/research/spectralatlas/webatlas.html.

[9] J. Anderson, 2013, http://www.stsci.edu/list/wfc3/tools/cte_tools.

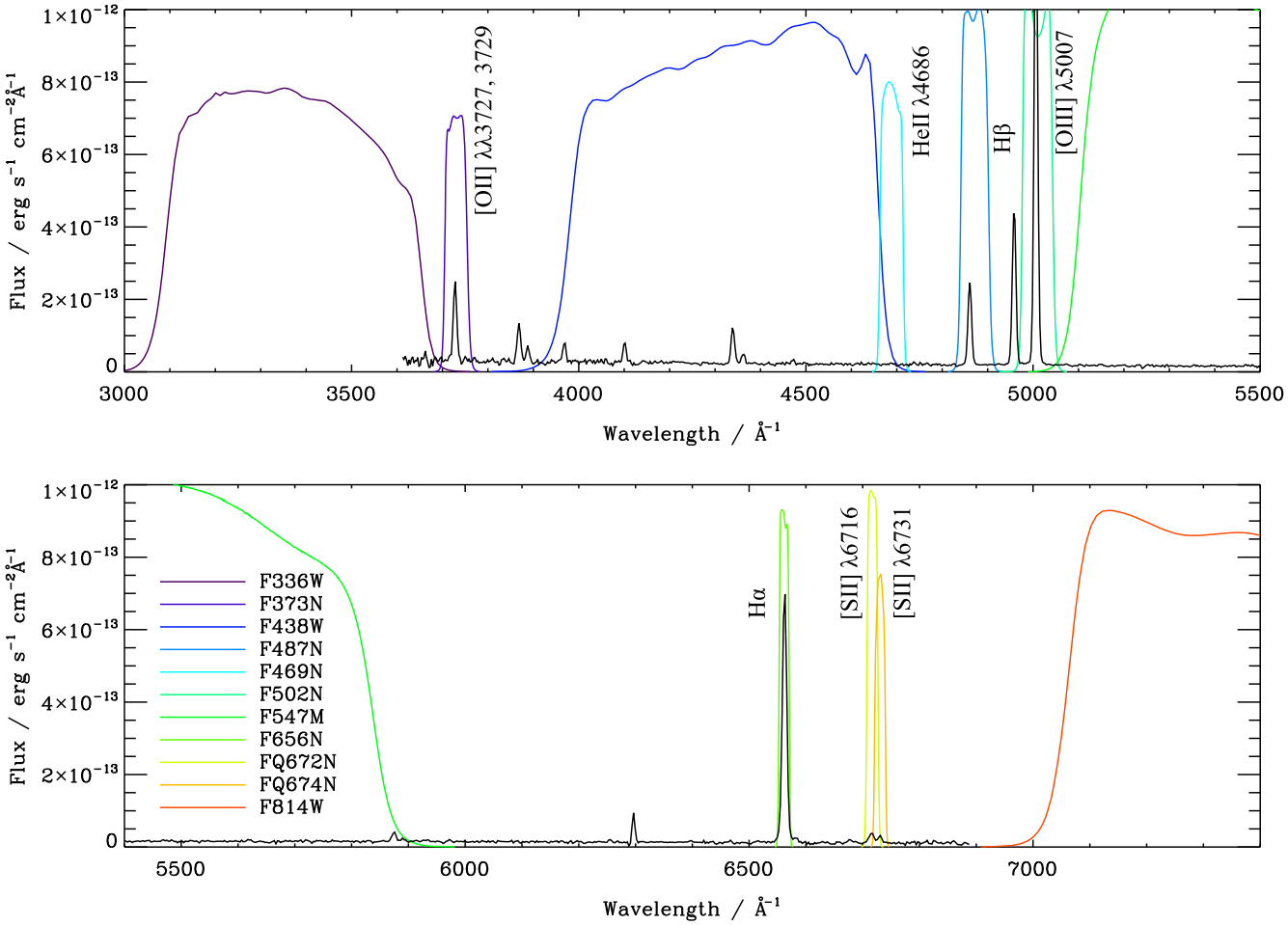

Figure 2. Filter transmission curves of each WFC3 filter utilized within this study overlaid on an optical spectrum of Mrk 71 from Moustakas & Kennicutt (2006) (described in Section 3.2). Transmission curves were scaled arbitrarily to match the flux level of the spectrum.

Figure 2). In particular, F656N exclusively covers Hα and only a negligible contribution from [N II] λ6584 is expected. Nebular lines do not provide any significant flux in the F336W and F547M filters, but there is a small contribution to the F814W filter (predominantly from [S III] and the Paschen series). To determine what effect this might have on the continuum subtraction, we use the near-infrared spectrum presented in Izotov & Thuan (2011) to quantify the nebular line contribution to the F814W flux. We find that less than 20% of the flux is due to nebular emission, and using a scaling based on the Hα image and repeated continuum subtraction, the [S II] flux is increased by less than 0.02 dex.

Traditionally, narrowband images are corrected for the stellar continuum using linear interpolation and extrapolation from neighboring continuum (i.e., broadband) images. However, here we adopt an alternative approach that exploits the wide wavelength coverage of the set of broadband filters at hand. We use the F336W, F547M, and F814W images to determine a spatially resolved stellar SED by fitting a linear combination of Bruzual & Charlot (2003) stellar population models to each pixel. We then calculate and subtract the contribution of these SEDs to the emission in each of the narrowband images, leaving just the (presumed) nebular emission. Finally, to determine the emission-line fluxes, we multiply normalized Gaussian SEDs by the narrowband filter transmission functions and divide these "normalized line fluxes" into the continuum-subtracted images to calculate the actual amplitudes of the emission lines. We have done this assuming a range of line widths from 70 to 150 km s^{-1} and find that the fluxes vary by only a few percent. To investigate the robustness of our continuum subtraction, we have also performed the continuum fitting using STARBURST99 models (Leitherer et al. 1999), which include nebular continuum emission, and find negligible changes to the calculated emission-line fluxes.

A color-composite image from the broadband filters is shown in Figure 1 alongside an image made from three emission-line images, which illustrates that our method has done an excellent job of removing the stellar emission.[10] We note that this methodology does not account for differences in the point-spread function between different filters, but this will not affect our subsequent analysis as we rebin the data to be larger than the point-spread function.

Hereafter each continuum-subtracted narrowband image will be referred to in terms of the emission-line flux that they cover, i.e., [O II], He II, Hβ, [O III], Hα, and [S II], with the latter being the sum of the two [S II] filters.

[10] It should also be noted that continuum subtraction was also performed using the method of Hong et al. (2014) and residual structure surrounding stellar emission in the continuum-subtracted images was seen to be larger than those created with the SED method described here.

Table 2
A Comparison between Emission-line Fluxes Measured from WFC3 Images and Those Obtained from Spectroscopic Studies within the Literature (Described in Section 3.2)

	WFC3 Images—Total	MK06		TI05		
Line ID	F_λ	F_λ	% Agreement	F_λ	F_λ Images	% Agreement
[O II]	129.00	142	91	25.12	22	88
He II	4.59	⋯	⋯	0.45	0.485	108
Hβ	176.00	220	80	51.95	46.6	90
[O III]	1130.00	1270	89	355.16	326	92
Hα	604.00	650	93	⋯	⋯	⋯
[S II]	18.7	43.8	43	⋯	⋯	⋯

Note. The spectroscopic results of Moustakas & Kennicutt (2006) were obtained by integrating over the entire galaxy and are therefore compared against fluxes summed over the entire WFC3 image. The long-slit observations of Thuan & Izotov (2005; TI05) were centered on the brightest region in Mrk 71. In this case we list the fluxes measured on the images within a simulated aperture (F_λ images). Observed fluxes (F_λ) are in units of 1×10^{-14} erg s^{-1} cm^{-2}.

3.1.1. Accounting for Emission-line Structure within the Filter

As discussed in Section 2, Mrk 71 is known to harbor both very broad emission lines and kinematical structure, two properties that can affect whether the emission lines are being fully covered by each of the filter bandpasses. In order to assess the magnitude of these effects on our measured emission-line fluxes, we simulated emission lines for a range of velocities and widths that represent the "worst-case-scenario" and measured the change in total flux seen within each narrowband filter. Velocities were chosen to range from 0 to 160 km s^{-1}, which accounts for both the systemic velocity of 90–100 km s^{-1} measured from optical emission line spectra (e.g., MK06 and Roy et al. 1991) and the H I velocity maps (Hunter et al. 2012) and an expansion velocity of 45 km s^{-1} measured by Roy et al. (1991) for the bubble surrounding cluster A. The model emission lines consisted of a narrow component with FWHM = 110 km s^{-1} and a broad component with FWHM = 2400 km s^{-1}, as measured by Roy et al. (1992) and Izotov et al. (2007), with the broad component being observed only in the [O III] $\lambda\lambda$4959, 5007 and Balmer lines. Changes in the velocity had a negligible effect on the emission lines in all cases, i.e., <1%. The emission-line width had a larger effect, most notably for Hα because the F656N filter is particularly narrow in order to miss [N II] λ6584. However, since the broad-component emission is known to contain <2% of the total emission-line flux for each line (Izotov et al. 2007), this effect is also negligible on our measured emission-line fluxes.

3.2. Comparison of Fluxes with Literature

In order to test the accuracy of our continuum-subtraction method, the fluxes in the final, emission-line images were compared with fluxes from ground-based spectra from the literature. Two comparison spectra are available to us: (1) Integrated spectrophotometry from MK06, where fluxes are obtained via a drift-scanning technique and integrated over a 90 × 60 arcsec^2 galaxy (Mrk 71 = ID 96 within their study). These fluxes provide the most accurate comparison with the total flux integrated over each image, i.e., removing any possible slit-loss effects. (2) MMT optical long-slit observations (extracted over a 6″ × 2″ aperture centered on the brightest part of the galaxy) published by Thuan & Izotov (2005, hereafter TI05). Here the authors extract fluxes from three different H II regions in the same galaxy, although the specific positions of these regions and the position angle (PA) of the slit are not given. As such, we use the summed fluxes from all three regions for comparison with a simulated 6″ × 2″ aperture centered on the brightest region of Mrk 71.

The fluxes from each of the observations of MK06 and TI05 are shown in Table 2. For each observation, we also list the flux measured from our emission-line images using the same extraction aperture (to our best knowledge). It can be seen that we are in very close agreement with the spectroscopic fluxes from the literature, obtaining >80% in all emission-line images, with the exception of [S II], for which there appears to be a discrepancy by a factor of two. As the two observations represent both the total flux (MK06) and the core flux (TI05) within Mrk 71, and a good agreement is found in both cases, we are confident that both our flux calibration and continuum subtraction have been successful in creating reliable emission-line images.

4. RESULTS

Before beginning our analysis, emission-line images were binned by 3 × 3 pixels. The final pixel scale is 0.″12, or ∼2 pc. Using the uncertainty in each pixel, we clip each image by 3σ in order to keep the highest-S/N pixels (and most reliable information), with the exception of He II, where we clip by 1σ (this line is particularly faint, and any deeper rejection cuts would remove most of the "WR" signature emission).

The final, continuum-subtracted images in emission lines Hα, Hβ, [O II], [O III], He II, and [S II] are shown in Figure 3. Both NGC 2366-II and Mrk 71 are seen in all emission-line images, with the exception of He II, which is only observed in Mrk 71. Cluster A (a super star cluster) is clearly defined in the western part of Mrk 71 with a shell of surrounding emission. The ionized gas within several smaller clusters is also seen throughout Mrk 71, as traced by the majority of the emission lines. The eastern part of Mrk 71, containing cluster B, is ∼9″ (∼150 pc) away from cluster A and has a sharp edge of emission ∼0.″5 (∼8 pc) wide along its eastern side, suggestive of a shock front. A large "arm" of emission is seen to extend north from cluster B, ∼2″ (∼45 pc) in width. The emission in Hα, Hβ, and [O III] is seen to extend further than that of [O II] and [S II]. We discuss He II emission in detail in Section 4.3.

Also shown in Figure 3 is the C(Hβ) image, i.e., extinction image created from the Hα/Hβ Balmer line ratio and adopting the case B recombination ratio $F(\mathrm{H}\alpha)/F(\mathrm{H}\beta) = 2.87$ (appropriate for gas with T_e = 10,000 K and N_e = 100 cm^{-3}), and the Large Magellanic Cloud (LMC) extinction curve

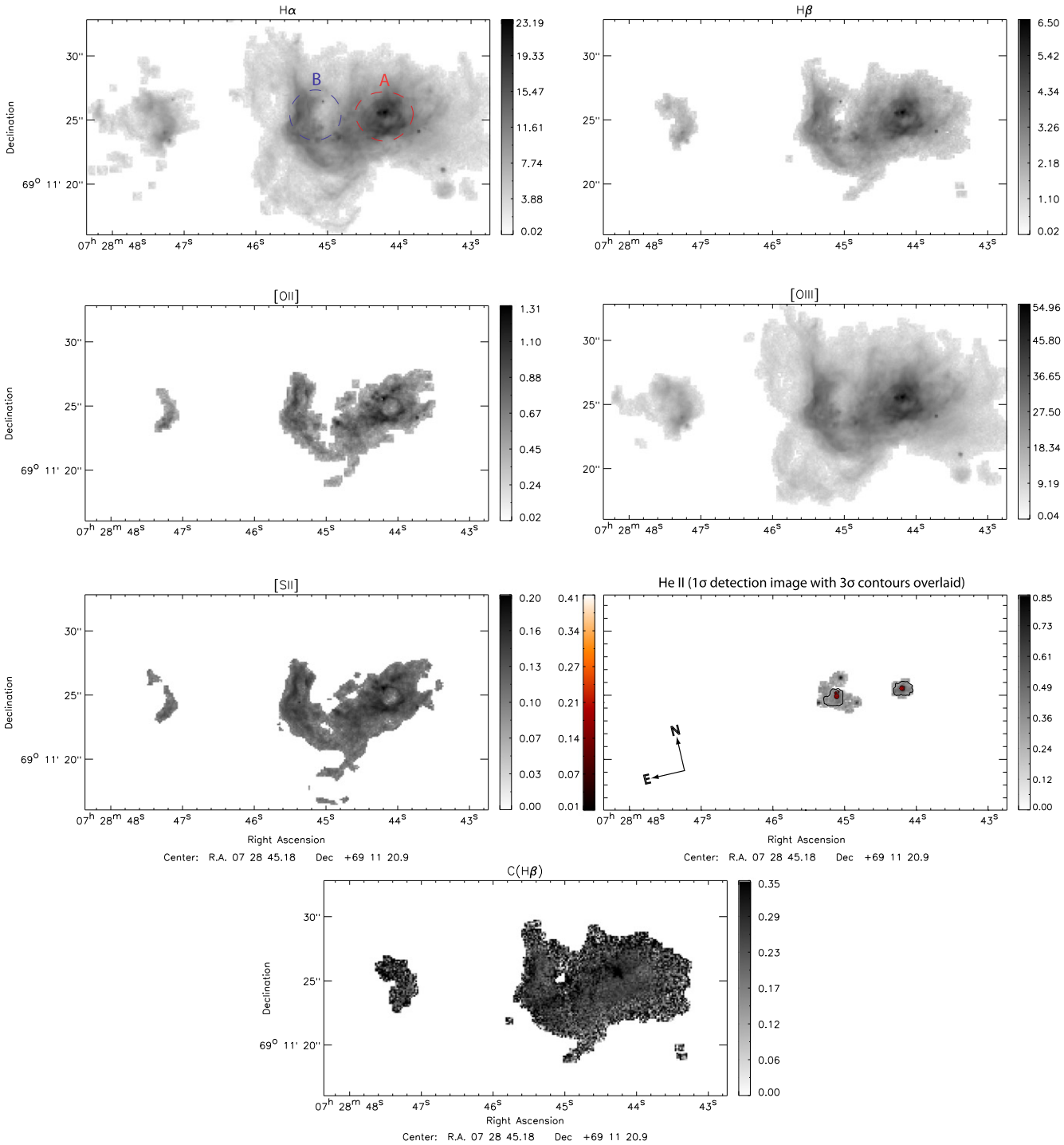

Figure 3. Continuum-subtracted emission-line images of Mrk 71 corresponding to the narrowband observations listed in Table 1. Fluxes are in units of 1×10^{-15} erg s^{-1} cm^{-2}. Each map shows 3σ pixel detections after 3×3 pixel binning, with the exception of He II, which shows 1σ detections after 3×3 pixel binning. We overlay the 3σ detected He II flux as contours in the He II panel (with 50% of the peak flux masked). The bottom panel shows the C(Hβ) image of Mrk 71, used to correct each narrowband image for reddening when necessary. Each emission-line image is normalized to its peak flux. Apertures overlaid on the Hα image denote the spatial extent of regions A and B, which are referred to in Section 4.

(Fitzpatrick 1999). It should be noted that any stellar photospheric absorption affecting the Balmer lines was corrected for during the SED-based continuum subtraction (Section 3.1). On average, we find that the Balmer decrement implies an average C(Hβ) = 0.13 ± 0.04 ($E(B-V)$ = 0.18 ± 0.06). In order to minimize the introduction of noise within the emission-line images, we only correct for reddening when necessary (i.e., when ratioing emission-line images that differ substantially in wavelength).

In Figure 4 we compare the morphology of emission in the forbidden lines, [O III] and [S II], with that of the Balmer line emission, Hβ. In each case it can be seen that the overall morphology of the two emission lines closely traces one another, with peaks in flux surrounding cluster A and along the

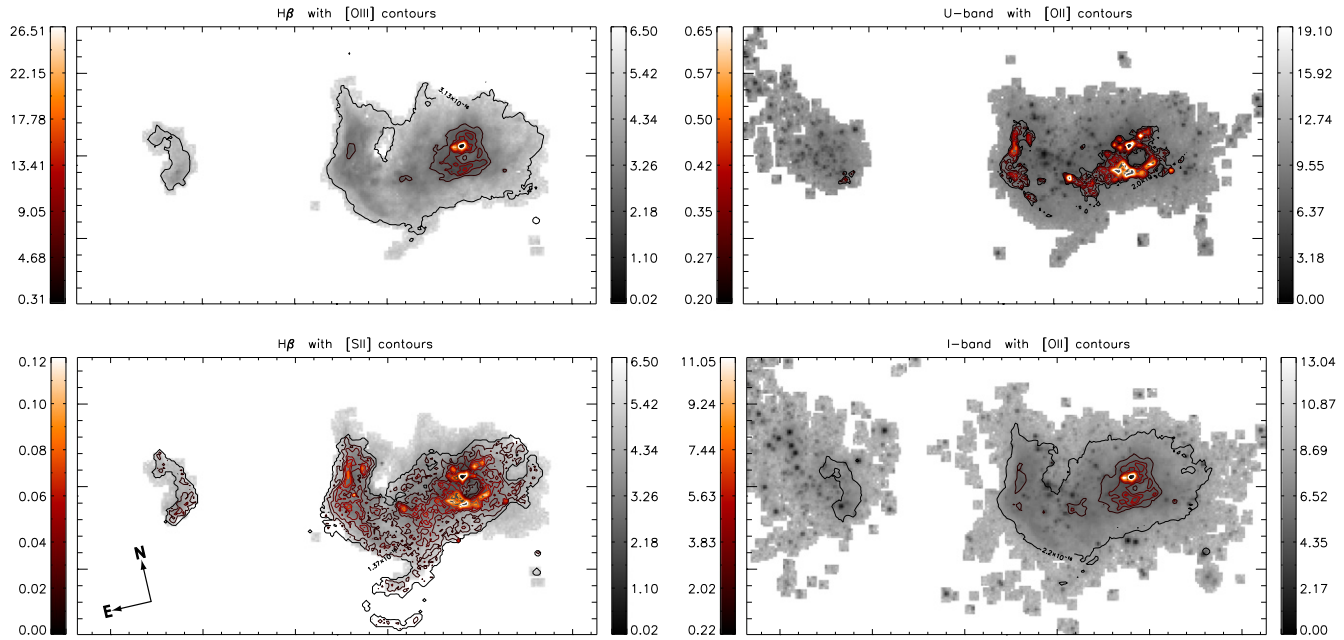

Figure 4. Left panels: comparison between the morphology of Balmer line and forbidden line emission throughout Mrk 71: Hβ emission line image with [O III] (top) and [S II] (bottom) contours overlaid. Right panels: emission-line morphology of Mrk 71 in relation to the stellar continuum emission—*U*-band image with [O II] contours overlaid (top); *I*-band image with Hα contours overlaid (bottom). For each contoured image we mask 50% of the peak flux in order to show the low-level forbidden line emission. Fluxes are in units of 1×10^{-15} erg s^{-1} cm^{-2}.

eastern edge of the arm, although the extent of Hβ and [O III] emission is larger than [S II]. The morphologies of [O III] and [S II] differ somewhat in the regions surrounding cluster A, where the lower ionization line, [S II], shows a pronounced shell around the cluster and the [O III] emission is more localized. This could be interpreted as seeing the edges of an ionized bubble of gas, $\sim$22 pc in diameter, which can be thought of as a single H II region or Strömgren sphere. However, the main ionizing source in cluster A is not seen in the center of this "bubble"—it instead lies on the northern edge of the ring (i.e., coincident with the strongest peak in [O III]). This scenario is in line with Drissen et al. (2000), who perceive cluster A to be a dense star cluster still embedded in dust and in its early stages of formation (i.e., $<$1 Myr).

Cluster A's location within the periphery of the bubble, combined with its young age and compact nature, may imply that this is a localized region of star formation that was triggered by the bubble itself, i.e., representing a second generation of star formation. Although there are no signs of an older cluster of star formation within close proximity to the bubble (Figure 1), its existence cannot be ruled out as it may have simply dispersed. However, we can address this scenario via the age of the bubble. Following the methodology of Martin (1998), if we assume a typical expansion velocity of 50 km s^{-1}, the bubble would have a dynamical age of $\sim$0.3 Myr, i.e., quite in line with the age of cluster A. Also, in order for the bubble to have triggered a 1 Myr old cluster, it would need to be traveling at $\ll$10 km s^{-1}. Overall, in consideration of the short timescales involved in both cluster A and the bubble, the most probable scenario is that they are associated with one another.

4.1. Emission-line Diagnostic Imaging

The line diagnostic diagram from nebular line emission, [O III] λ5007/Hβ versus [S II](λ6716 + λ6731) (or [N II] λ6584/Hα), has been used to study the starburst or AGN activity in galaxies (Baldwin et al. 1981, hereafter BPT; Kewley et al. 2001, hereafter K01) and to investigate the ionized gas structure of the ISM for resolved regions (e.g., Calzetti et al. 2004; Westmoquette et al. 2007; Hong et al. 2011). These emission-line diagnostics are successful in separating different sources of ionization because the relative intensity of the two collisionally excited lines, [S II] and [O III], depends on the shape and strength of the ionizing radiation (along with the metallicity of the ISM), whereas the Balmer recombination lines have the same dependence on the photoionization process and are used only to normalize out the ionizing luminosity. For example, in photoionized gas, as the number of high-energy photons increases, there is an increase in [O III] emission and a decrease in [S II] emission (due to the increase in doubly ionized sulfur). This effect can be seen in Figure 5, where we show Mrk 71 in pixel-by-pixel [S II]/Hα and [O III]/Hβ emission line ratios. In the gas surrounding cluster A there is a peak in [O III]/Hβ, whereas [S II]/Hα can no longer be seen. Then moving away from the strong photoionizing emission from the OB stars within cluster A, [S II]/Hα increases while [O III]/Hβ decreases.

Interesting additional structure can also be seen in these emission-line ratio images. First, directly above cluster A, a strip of highly ionized gas can be seen directly alongside a strip of low-ionized gas (i.e., decreased [O III]/Hβ as highlighted with the red dashed box), which is also mirrored in the [S II]/Hα image. This structure is suggestive of an ionization front from highly ionized gas being blown away from the hot OB stars in the main cluster. Second, the eastern edge of the arm is traced by an increase in [S II]/Hα and a decrease in [O III]/Hβ, signifying a sharp transition between high and medium ionized gas. A similar structure can also be seen along the edge of NGC 2366-II. The morphology and sharp gradients of these emission-line ratios suggest the existence of shocked gas along the eastern edge of the arm as the gas moves away from cluster B and shocks against the surrounding ISM.

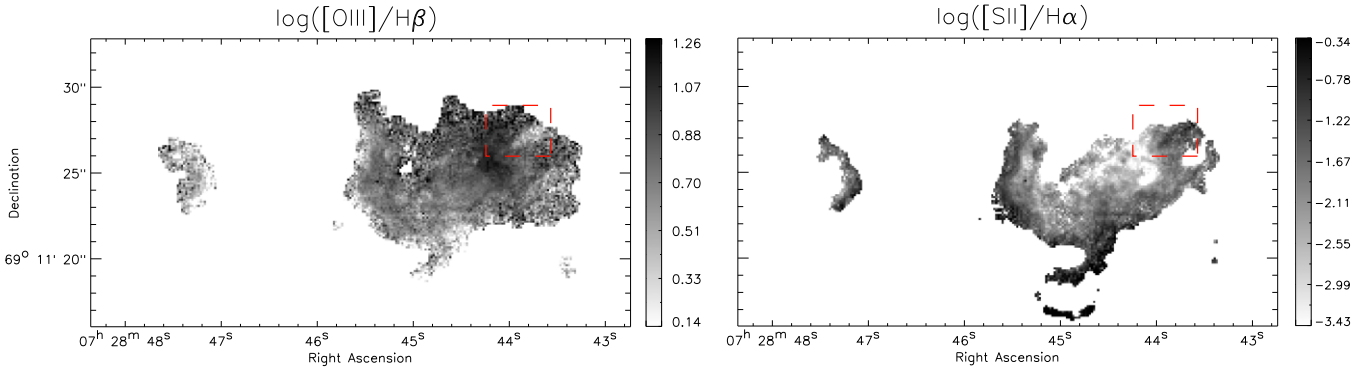

Figure 5. Imaging BPT emission line diagnostics across Mrk 71: the emission-line ratio of [O III]/Hβ (left) and [S II]/Hα (right). The red dashed box highlights a region of highly ionized gas alongside low-ionized gas, i.e., structure suggestive of an ionization front (see the text for details).

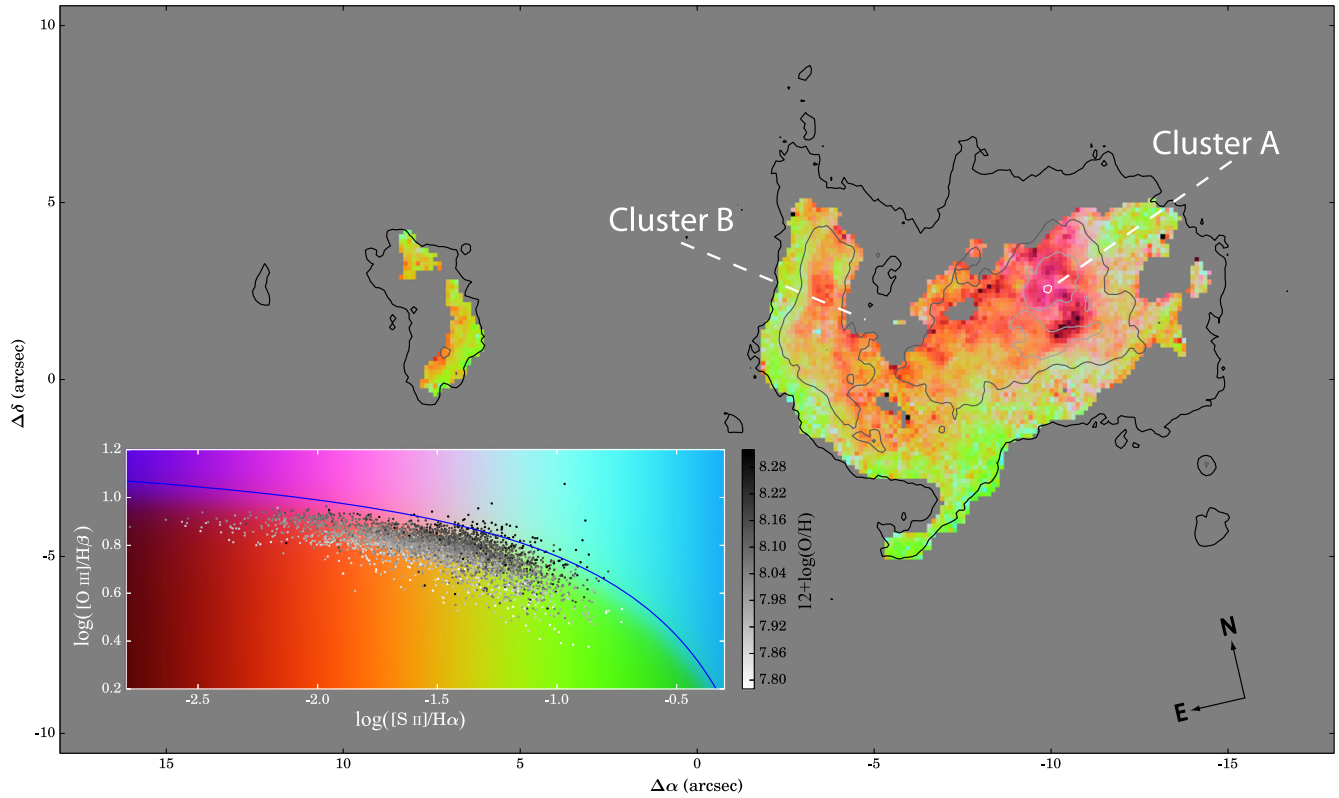

Figure 6. Emission-line diagnostic map showing log([S II]/Hα) vs. log([O III]/Hβ), derived from the line ratio images in Figure 5 and color-coded according to their location within the BPT diagram, shown in the inset. Overlaid contours represent the morphology of Hα emission (Figure 3). The grayscale of the data points overlaid in the BPT diagram (inset) indicates their metallicity (as discussed in Section 4.2). The "maximum starburst line" from Kewley et al. (2001) is overlaid in blue.

In order to explore the excitation mechanisms fully, in Figure 6 we plot both line ratio images in a color-coded diagnostic parameter space as [S II]/Hα versus [O III]/Hβ. Also shown is the "maximum starburst line" from K01, above which the line ratios cannot be due to photoionization alone, demonstrating that the large majority of the gas within Mrk 71 and NGC 2366-II is in fact photoionized. Alternatively, the photoionized emission may be dominating over shock excitation, despite the 2 pc pixel^{-1} resolution. However, if the superbubble surrounding Mrk 71 is expanding at only 45 km s^{-1} (Roy et al. 1991), the lack of shock-excited emission is perhaps not surprising. We additionally color-code the pixels overlaid in the BPT diagram according to their metallicity (discussed in Section 4.2). A gradient in metallicity can be seen in the direction of [O III]/Hβ and follows the shape of the maximum starburst line. Figure 6 contains a wealth of information about the ionization throughout Mrk 71. First, we can clearly see that Mrk 71 has a very inhomogeneous ionization structure, where cluster A occupies a region of higher [O III]/Hβ and lower [S II]/Hα than cluster B, and the lowest [O III]/Hβ and [S II]/Hα lie in the galaxy outskirts. The morphology of the strong [O III]/Hβ line ratio in cluster A aligns with the peak in Hα emission (overlaid grayscale contours). The gradient of decreasing [O III]/Hβ as you move away from cluster A appears to support the findings of Drissen et al. (2000), who suggest that cluster A provides the bulk of the ionizing flux for the entire Mrk 71. However, while the gradient is strong in the west-to-south direction from cluster A, it is significantly more shallow in the opposite direction, i.e., toward cluster B. This suggests that the gas throughout Mrk 71

may be receiving a non-negligible contribution of ionizing photons from Cluster B also. The ionizing source and physical conditions of both clusters are explored further in the following section.

4.1.1. Photoionization Models

We investigate the properties of the ionized gas further using MAPPINGS V[11] (R. Sutherland et al. 2015, in preparation). Separate models for clusters A and B are constructed in order to account for the different stellar populations within them (Section 2) and subsequent chemical and physical conditions. A number of constraints were used to tailor the model for each cluster using both the data presented here and information from previous studies.

For each cluster, we run a grid of spherical, isobaric H II region models at metallicities of 0.15 and 0.2 $Z_{\odot}$ (which represent the elemental abundances measured by Izotov et al. [1997], where abundances are given for both clusters separately). We adopt ionizing luminosities of log $(L_{\mathrm{H}\beta}) = 39.2$ and 38.7 erg s^{-1} for clusters A and B, respectively (as measured from our reddening-corrected Hβ images using the cluster apertures shown in Figure 3). In order to match the He II/Hβ ratios of each cluster ($(9.34 \pm 6.06) \times 10^{-3}$ and $(7.81 \pm 5.16) \times 10^{-2}$ for clusters A and B, respectively), it was necessary to use input spectra for non-LTE stellar atmospheres from Rauch (2003) with effective temperatures of 90 and 105 kK, respectively.

Grids were initially run for pressures between $P/k = 10^5$ and 10^8, where k is the Boltzmann constant, until the electron density of each cluster was matched. The range in pressure is equivalent to that of density, as the temperature remains fixed at $T = 1 \times 10^4$ K. The electron density (N_{e}) spatial profiles from Pérez et al. (2001) using [S II] $\lambda6716/\lambda6731$ show averages of $N_{\mathrm{e}} = 300$ cm^{-3} and 100 cm^{-3} for clusters A and B, respectively, which were reproduced by models at log$(P/K) = 7$ and 6.5, respectively.

Once the pressures were constrained for each cluster, the inhomogeneous nature of the nebular gas seen in Figure 6 was recreated by running each metallicity model for a range of the ionization parameters, U (which represents the density ratio of ionizing photons to particles), between log$(U) = -3$ and -1 in steps of $\Delta U = 0.5$ and terminating them between a range of optical depths (τ) between $\tau = 5$ and 80 in steps of $\Delta\tau = 15$. The range of ionization parameters was chosen to encompass the average U-parameter for each cluster, log $(U) = -1.89 \pm 0.3$ and -2.12 ± 0.23 for clusters A and B, respectively, derived from the [O III]/[O II] ratio image (discussed and shown in Section 4.3) and the metallicity of each cluster using the relations of Kewley & Dopita (2002).

We overlay the photoionization grids on BPT diagrams in Figure 7, which show both clusters on a pixel-by-pixel basis. For comparison with non-photoionization excitation, we also show the emission-line ratios predicted by the shock+precursor models generated by MAPPINGS III by Allen et al. (2008), at LMC metallicity (the closest in metallicity to that of Mrk 71). A minimum offset of ~0.7 dex is seen between the observed [S II]/Hα emission line ratios and the shock models. As this cannot be accounted for by the possible oversubtracted continuum in the [S II] image (as discussed in Section 3.1), it appears that the gas within Mrk 71 is predominantly photoionized. For both clusters, a large majority of line ratios are successfully reproduced by the U and τ grids between 0.15 and 0.2 $Z_{\odot}$, i.e., the gas appears to be dense, with log $(U) = -2.5$ to -1, and ranging from optically thin to thick. In cluster A, the points with log([S II]/Hα) < -2, which are clustered in a shell-like structure (Figure 6), lie at the optically thin and low-metallicity end of the grid, suggesting that this region should have a particularly high surface brightness. The points that lie below the grids could be due to the fact that we are integrating through a line of sight off the center of the cluster rather than directly out (like the photoionization models). In this scenario, it is possible to see an [O III]/Hβ ratio that is characterized by a larger effective optical depth, while still missing the lower ionization region entirely and showing lower [S II]/Hα ratios. For cluster B the model grid lies at lower [O III]/Hβ line ratios as it is generated at a slightly lower pressure (=electron density) and the points do not extend down to the low [S II]/Hα values observed in cluster A. Our best-fit models suggest that both clusters are dense regions of intense star formation, with metal content ranging from 0.15 to 0.2 $Z_{\odot}$ and a clumpy, dusty medium. These findings are in agreement with the UV models of Drissen et al. (2000), which suggest that cluster B is 2.5–5 Myr old and contains a population of massive O- and B-type stars, while cluster A is younger (<1 Myr), in the ultracompact H II region stage, and shrouded by dust, where newly formed stars are still embedded in their natal molecular clouds.

4.2. Metallicity Imaging

Our extensive set of narrowband imaging also allows us to investigate the distribution of metallicity (i.e., oxygen abundance, O/H) throughout Mrk 71 and NGC 2366-II. For this we use the R_{23} index, an index first proposed by Pagel et al. (1979) and now the most widely used approximate indicator of the oxygen abundance in star-forming galaxies, based on the ratios of what are typically the strongest emission lines from H II regions at visible wavelengths: $R_{23} \equiv [I(3727) + I(3729) + I(4960) + I(5008)]/I(\mathrm{H}\beta)$.

One drawback of this index is that a reddening correction is required, since the lines in question are spread over ~1300 Å. We therefore correct each emission-line image using the extinction image shown in the bottom panel of Figure 3. In deducing the metallicity distribution from the de-reddened emission-line images, we made use of the analytical expressions by McGaugh (1991) as given by Kobulnicky et al. (1999). These expressions take into account the effect of the ionization parameter on the relationship between R_{23} and O/H by including a term that depends on the ratio of the [O II] and [O III] lines, $O_{32} \equiv [I(4960) + I(5008)]/[I(3727) + I(3729)]$.

Another, and perhaps the most major, drawback of this index is that the relationship between R_{23} and O/H is double valued, so that other line ratios are required to break the degeneracy. Unfortunately, other metallicity-dependent line ratios, such as [N II]/Hα (Pettini & Pagel 2004), are not available here. However, we do have O/H measurements from the aforementioned long-slit observations (Section 3.2) at our disposal, which we can use to break this degeneracy for the following reason. In Figure 8 we plot the upper- and lower-branch relations of the R_{23} index against oxygen abundance. Overplotted are the metallicities derived from these two relations using pixels from the R_{23} image. We also show the oxygen abundance calculated by TI05, 12 + log(O/H) = 7.89 ± 0.1,

[11] Available at miocene.anu.edu.au/Mappings

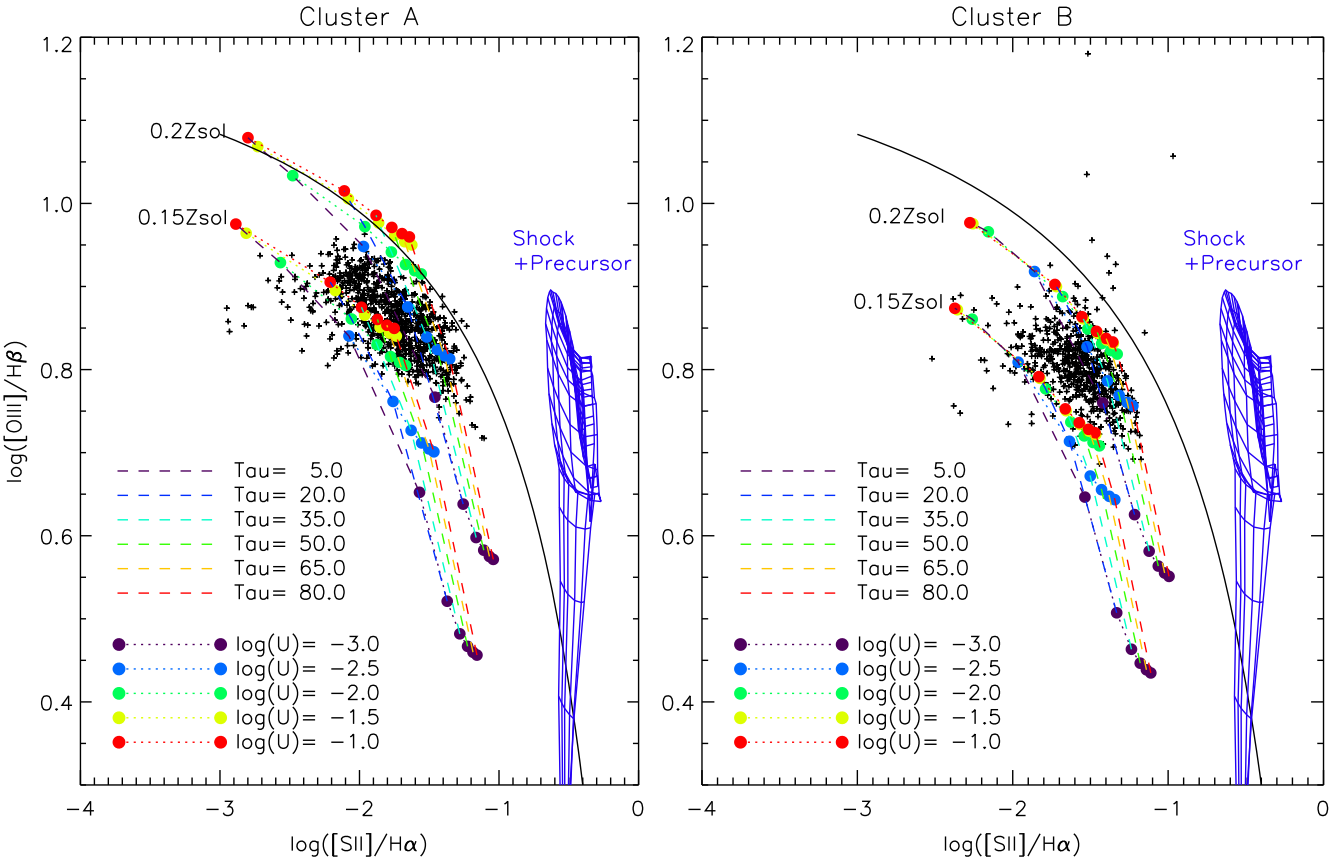

Figure 7. Pixels corresponding to the separate regions of gas surrounding clusters A (left panel) and B (right panel). The spatial extent of these regions is denoted in Figure 3. Overlaid are the customized photoionization model grids described in Section 4.1.1, which cover 0.15 and 0.20 $Z_{\odot}$, ionization parameters of $\log(U) = -3$ to -1, and optical depths of $\tau = 3$–103. We also overlay the shock+precursor models at LMC metallicity from Allen et al. (2008) (blue solid lines) and the "maximum starburst line" from Kewley et al. (2001) (black solid line).

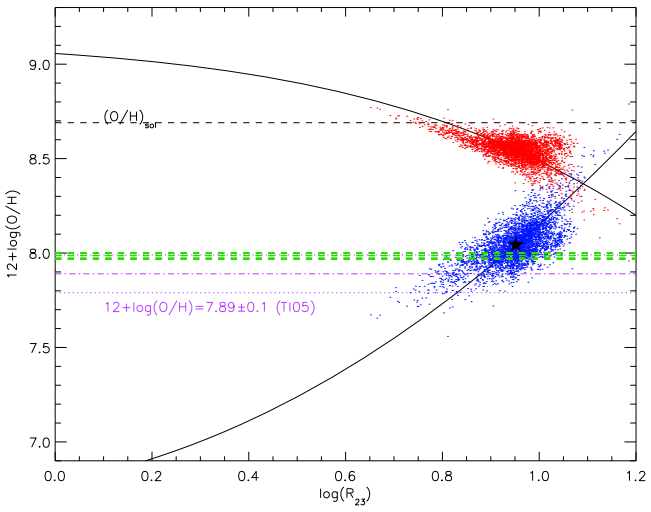

Figure 8. R_{23} emission-line ratio as a double-branched function of metallicity (solid black lines). The overlaid red and blue points are pixels in the R_{23} (i.e., ([O III] + [O II])/Hβ) emission-line image of Mrk 71, corresponding to "upper" and "lower-branch" metallicities, respectively. Also shown are the direct-method metallicity and its uncertainty derived from long-slit spectroscopic observation of TI05 (purple dot-dashed and dotted lines, respectively), which suggests that the metallicity distribution of Mrk 71 lies on the lower branch. The mean metallicity derived from our lower-branch R_{23} images is represented by a black star. Green dashed lines indicate the R_{23} lower-branch metallicities derived from the emission-line fluxes of TI05 (long-slit) and MK06 (integrated).

using the "direct method" (a highly accurate method that utilizes the electron temperature of the gas), which crosses the lower branch of the R_{23} index.

An offset of approximately -0.15 dex exists between the direct-method abundance of TI05 and the mean R_{23} metallicity calculated from our images (shown as a black star). This offset is not unexpected—direct-method abundances are often found to be slightly lower than those calculated from strong-line indices, which we typically attribute to model uncertainties, temperature fluctuations, and/or deviations from thermal electron distributions (see, e.g., Belfiore et al. 2015, and references therein). To check that the discrepancy is not due to our emission-line ratios, we also plot the lower-branch R_{23} metallicities as derived from the emission-line fluxes of TI05 and MK06 (green), which are seen to be in agreement with our distribution along the lower branch. Further evidence that the O/H abundance of Mrk 71 lies on the lower branch of the index can be found in the emission-line diagnostic diagram shown in Figures 6 and 7, where the emission-line flux ratios lie in regions typically occupied by low-metallicity objects (see, e.g., Dopita et al. 2013).

Once convinced that Mrk 71 metallicities are represented by the lower-branch R_{23} index, we create a "metallicity image" of Mrk 71, which we show in Figure 9. While the index-based metallicities may not represent the "absolute" metallicity of the gas, we can use this image to investigate the distribution of metallicity throughout Mrk 71 and determine whether or not

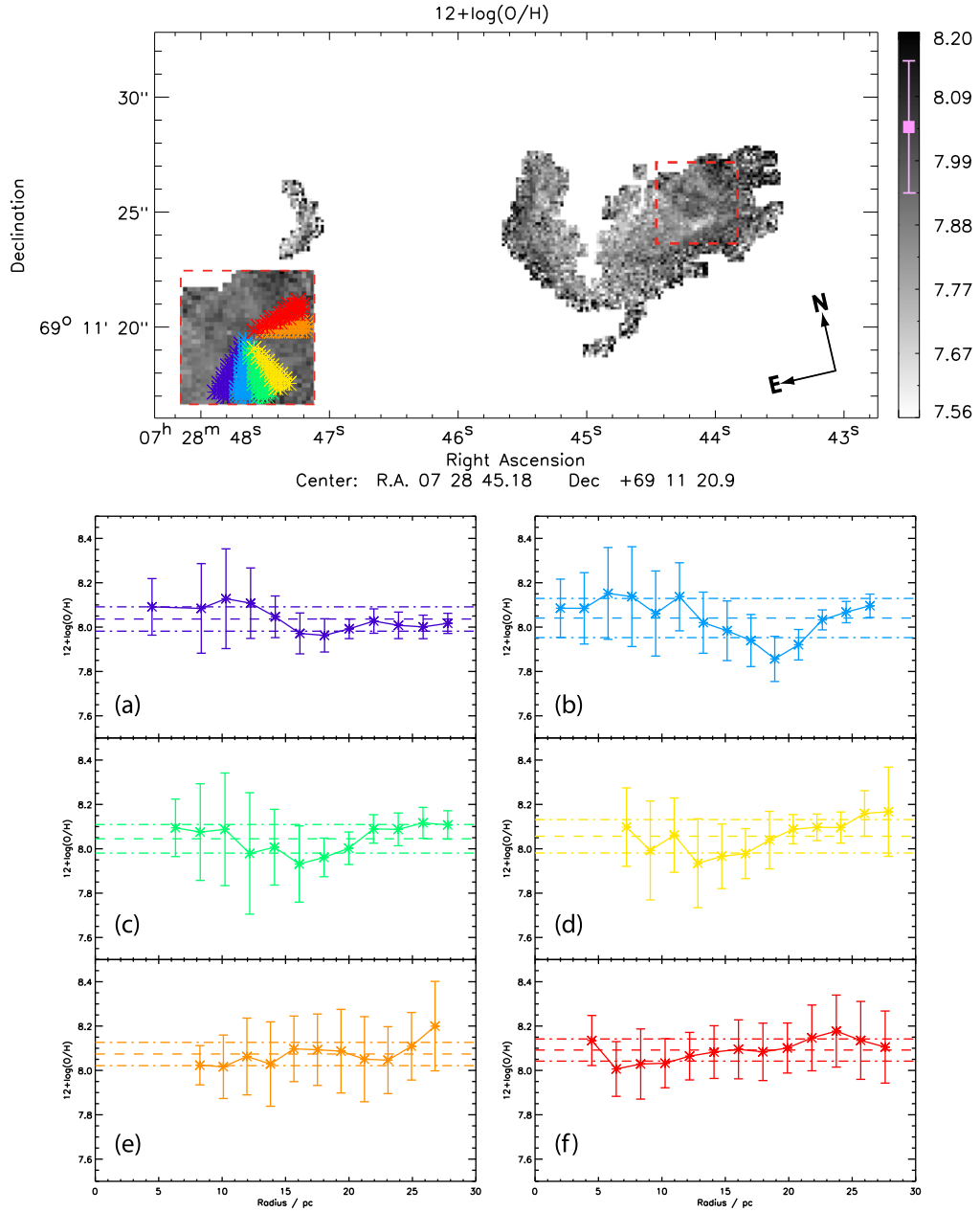

Figure 9. Top panel: "metallicity image" of Mrk 71, corresponding to the lower branch of the R_{23} diagnostic. The pink data point shown within the color bar represents the average metallicity and 1σ distribution derived from the image, $\langle 12 + \log(\mathrm{O/H}) \rangle = 8.04 \pm 0.11$. Lower panels: radial cuts from the center of the highlighted region (red dashed box and also shown on a larger scale in the inset). Each profile represents the average metallicity in each radial bin along each colored segment shown in the inset and incorporates the total uncertainty in 12+log(O/H). Each segment's average metallicity and 1σ distribution are shown overlaid as dashed and dot-dashed lines, respectively.

Mrk 71 is chemically homogeneous. From all pixels within Figure 9 we calculate a mean of $12 + \log(\mathrm{O/H}) = 8.04 \pm 0.11$ (represented by the data point within the figure's color bar). If we compare this average metallicity to the distribution of metals shown in Figure 9, we can see not only that Mrk 71 is chemically inhomogeneous but also that a number of interesting chemical structures can be seen in the O/H dispersal throughout the system.

First, the gas appears to increase in metallicity with increasing distance from cluster B. This positive gradient is seen most clearly across the edge of the arm that extends northward from cluster B, a region ∼45 pc across. The gradient is also mirrored in NGC 2366-II. Positive, or inverted, metallicity gradients are relatively rare and have so far been attributed to interaction and/or metal-poor gas falling into the center of the system (Cresci et al. 2010; Queyrel et al. 2012; Sánchez Almeida et al. 2014). While we are yet to detect inflowing gas toward Mrk 71, [O III] and H I maps do suggest that it is interacting with NGC 2363 (not covered here), ∼1.4 kpc northwest of Mrk 71 (Roy et al. 1991; Braun 1995).

Second, there is a ring-shaped decrease in metallicity surrounding cluster A (∼26 pc in diameter and highlighted by a red dashed box). We investigate the authenticity of this structure in the lower panels of Figure 9, where we show radial cuts from the center of the highlighted region (as shown in the inset). Each cross-section profile represents the average

metallicity in each radial bin along each colored segment and incorporates the total uncertainty in 12 + log(O/H). It can be seen that in segments covering the most pronounced part of the ring-shaped structure (i.e., the lower edge of the ring, panel (b)) the decrease in metallicity is over a ∼5–10 pc distance and exists outside the uncertainties in each bin. However, in less pronounced areas of the ring the gas appears to be chemically homogeneous within the uncertainties.

If we consider the young (<1 Myr) age of cluster A, this lower ring of low-metallicity gas may be interpreted as gas that is yet to be enriched by the stellar population within the cluster. However, this scenario would not explain how the metallicity then increases outside the ring. A similar scenario has also been witnessed in NGC 5253, a local starburst galaxy famous for hosting the first observed case of nitrogen enhancement (e.g., Walsh & Roy 1989; Kobulnicky & Skillman 1997; López-Sánchez et al. 2007; Westmoquette et al. 2013). Like Mrk 71, the chemical inhomogeneity in NGC 5253 lies very close to a region hosting extremely young ($\lesssim$1 Myr) star clusters (Calzetti et al. 2015). This suggests that the extreme youth of the clusters may be playing a role here, i.e., the pollution from the most massive stars within the cluster has not yet mixed properly, and as a result we observe chemical inhomogeneities.

An alternative (and probably more likely) scenario is that here we are seeing a region in which the photoionization-model-based R_{23} diagnostic breaks down. Indeed, the ring of low-metallicity gas aligns well with the ionized-gas "bubble" traced by the strong [O II] and [S II] emission (Figure 3), which may signify a shock front. However, we know from Section 4.1 that non-photoionized gas does not exist in this region. It is perhaps instead due to the fact that strong-line diagnostics are designed to work over H II regions as a whole, i.e., where the emission is integrated over the sphere of gas photoionized by the central stellar source. As discussed in Section 4, the bubble blowout structure seen in this region is analogous to a single Strömgren sphere, and metallicity diagnostics such as R_{23} cannot be applied because it was calibrated over whole, or multiple, spheres of this kind. The diagnostic may not work correctly here because we are instead spatially resolving emission *across* the H II region.

4.3. He II Emission Line Imaging

The narrowband F469N observations were designed to locate the extent of He II λ4686 emission throughout Mrk 71. This emission has two contributing factors. First, WR stars can produce characteristic broad emission (FWHM $\gtrsim$ 1000 km s^{-1}) in specific ions or "WR features" (e.g., He II λ4686) that originate in the envelopes of massive stars undergoing rapid mass loss. Second, a narrow nebular He II λ4686 emission line (FWHM ∼ 100–300 km s^{-1}) can be superimposed on this broad feature. This line, with an ionization potential of 4 Ry, is often seen in the spectra of BCDs owing to the fact that the hardness of the ionizing radiation increases with decreasing metallicity (e.g., Campbell et al. 1986). The origin of nebular He II λ4686 has often been cause for debate (Thuan & Izotov 2005; Izotov et al. 2007; Kehrig et al. 2015), with suggestions including hot WR stars, shocks from supernovae, and X-ray binaries. Previous long-slit observations of Mrk 71 suggest that both broad and narrow spectral features may be present. One (out of three) optical spectra of Mrk 71 obtained by TI05, and shown in detail by Izotov et al. (2007), shows prominent WR features, whereas nebular He II λ4686 is

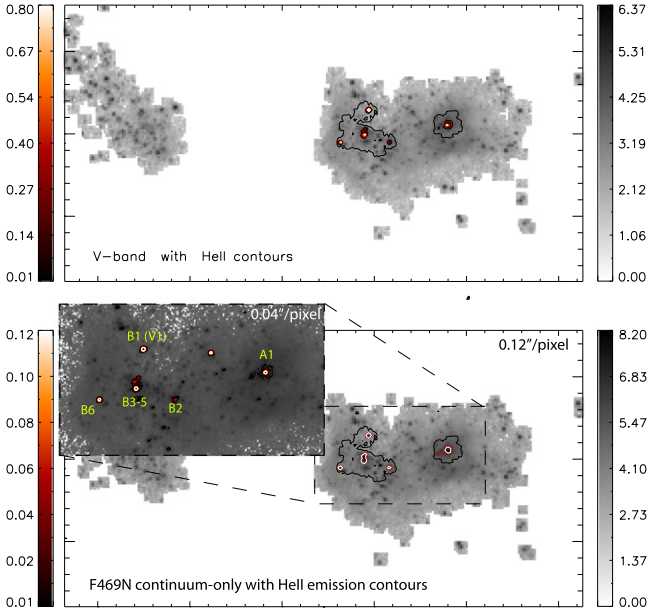

Figure 10. Comparison between the morphology of He II emission and *V*-band stellar continuum (top panel), and F469N continuum only (bottom panel). The inset shows the original (0.″04 pixel^{-1}) F469N continuum-only image with He II contours overlaid, which we use to resolve individual WR stars. For each contoured image we mask 50% of the peak flux in order to show the low-level emission. Fluxes are in units of 1 × 10^{-15} erg s^{-1} cm^{-2}.

observed in all three spectra. As we are unable to disentangle nebular from broad emission in our He II image, here we can only treat the combined emission as a tracer for highly ionized gas and WR stars.

The 1σ He II (continuum-subtracted) image is shown in Figure 3 (with 3σ contours overlaid), where localized emission can be seen in the two main stellar clusters—a strong peak associated with cluster A and another in and surrounding cluster B. Each peak of He II emission is 0.″12–0.″16 across, corresponding to 2–3 pc at the distance of Mrk 71. In order to explore the source of our He II detections, in Figure 10 we show the He II emission overlaid on the 1σ cut *V*-band image and F469N continuum-only image (i.e., a by-product of our continuum-fitting process). Both images show only the underlying stellar continuum, i.e., without WR or nebular He II emission, and it can be seen that each peak in He II emission aligns with stellar continuum features, suggesting that the emission is (at least) partly due to WR stars.

We label each peak of He II emission in Figure 11, according to the cluster in which it is located. The summed He II flux within a 1.″15 radius aperture for A1 and a 0.″7 aperture for B1–B6 is listed in Table 3, along with the corresponding luminosities (at a distance of D = 3.44 Mpc). If we inspect the original, unbinned He II image (i.e., at 0.″04 pixel^{-1}, inset of Figure 10), we can see that each aperture contains a single WR star, with the exception of B3-5, which contains a cluster of three WR stars. The additional peak in He II emission in the 0.″04 pixel^{-1} image (between the two clusters and unlabeled) is not visible in the 1σ cut 0.″12 pixel^{-1} image; as such we do not consider it as a reliable detection. We must also bear in mind that at the 3σ level (contours overlaid in Figure 3), He II emission is seen in only B3-5 and A1, suggesting that cluster B may only host three WR stars overall.

Using a similar method (i.e., F469N WFPC2 0.″05 pixel^{-1} observations), Drissen et al. (2000) also located three WR stars

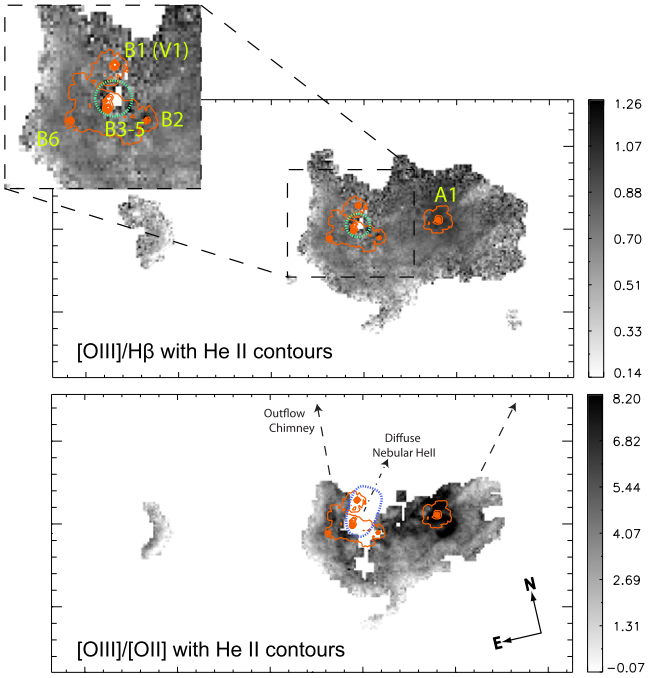

Figure 11. Morphology and strength of ionizing field throughout Mrk 71, with He II contours overlaid (orange). Knots of He II emission are labeled according to the clusters in which they lie, with corresponding fluxes given in Table 3. Top panel: [O III]/Hβ image, with an inset showing a zoom-in of the area defined by the black dashed box. This highlights a small blown-out cavity, ∼18 pc in diameter (green dotted circle), where no [O III] or Hβ exists. Bottom panel: [O III]/[O II], which corresponds roughly to the ionization parameter, U. Here we highlight a larger cavity, ∼28 pc across, where no [O II] emission exists (blue dotted ellipse). Both cavities align with the direction of extended nebular He II emission seen by Drissen et al. (2000) (dot-dashed arrow) and the "chimney" of outflowing gas discovered by Roy et al. (1991) (dashed arrow).

Table 3
He II Emission Measured within a Circular Aperture Centered on Knots of He II Emission Labeled in Figures 10 and 11

WR Region	Flux/$\times 10^{-15}$ erg s^{-1} cm^{-2}	L/ $\times 10^{36}$ erg s^{-1}
A1	5.88	3.01
B1[a]	3.58	1.84
B2[a]	1.44	7.38
B3-5	5.68	2.91
B6[a]	2.06	1.06

Notes. Each aperture has a radius of 0.″7, apart from region A with a radius of 1.″15.
[a] Not present at the 3σ detection level.

in cluster B at the location of B3-5, but no significant He II emission outside B3-5 or in cluster A. They attribute the latter to the fact that cluster A is too young to harbor a WR population and that the starlight is hidden by dust. However, this may also in part be due to an oversubtraction of their continuum image, which was created from a weighted average of F547M and F439W images, with the latter being contaminated by a number of emission lines (Figure 2). Drissen et al. (2000) also detect a WR star 150 pc north of cluster B, which we do not see in our 0.″04 pixel^{-1} or 0.″12 pixel^{-1} He II images.

We can investigate the nebular component of He II emission by comparing its morphology to that of the highly ionized gas in Mrk 71. The strength of the ionizing radiation can be

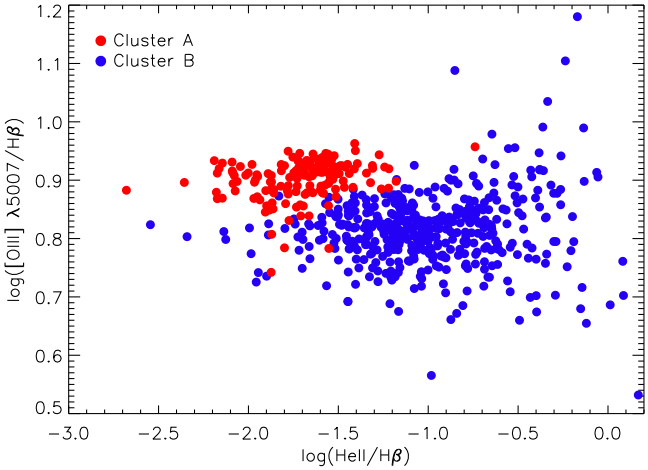

Figure 12. Distribution of He II/Hβ emission with regard to the degree of ionization, represented by [O III]/Hβ. Cluster A is seen to occupy a higher [O III]/Hβ ratio than cluster B, suggesting that He II emission in this region is from nebular+broad emission.

parameterized by [O III]/[O II] (created from reddening-corrected images) and [O III]/Hβ emission line ratios, which are shown in Figure 11 with He II contours overlaid. The most highly ionized gas is located around cluster A, from which large filaments of strong [O III]/[O II] are seen to extend. The strongest peak in He II emission aligns with the most strongly ionized gas (i.e., cluster A), whereas the emission along the arm and cluster B lies among relatively low ionization gas. Combined with its young age ($\lesssim$1 Myr; Drissen et al. 2000), this suggests that the He II flux detected in cluster A is most likely nebular in origin, whereas cluster B's emission is attributable to broad He II emission from WR stars. To illustrate this further, in Figure 12 we plot He II/Hβ versus [O III]/Hβ for regions of gas surrounding clusters A and B (regions are denoted in Figure 3). While no clear correlation exists between He II emission and the strength of the ionizing radiation, the two clusters do occupy different regions of this parameter space, with cluster A showing a higher [O III]/Hβ ratio than cluster B by ∼0.15 dex, demonstrating that cluster A does indeed have harder ionizing radiation than cluster B.

WR stars are known to harbor powerful stellar winds, with wind densities an order of magnitude higher than massive O stars, which can have a profound influence on the surrounding ISM (Crowther 2007). The inset of Figure 11 shows a zoom-in around cluster B where there is also a region (∼18 pc across, green dashed circle) of little or no [O III]/Hβ flux surrounding the brightest knot of He II emission. The lack of emission in this region is suggestive of a blowout cavity possibly caused by the winds from the B3-5 WR cluster. The cavity has a much larger extent for [O II] (28 pc across, blue dashed ellipse in lower panel of Figure 11) than [O III] and Hβ[12] and aligns well with the direction of extended nebular He II emission seen by Drissen et al. (2000) (their Figure 8) and the north–northwest orientation of the large "chimney" of outflowing gas discovered by Roy et al. (1991). It should also be noted that the WR stars in cluster B are also joined by dozens of OB stars (Figure 1; see also Drissen et al. 2000), which would contribute to the energy ejected into the ISM here, along with supernova explosions.

[12] This "gap" in emission-line flux also exists in the 1σ and 2σ cut [O II], [O III], and Hβ images, demonstrating that it is not simply due to lack of signal in this region.

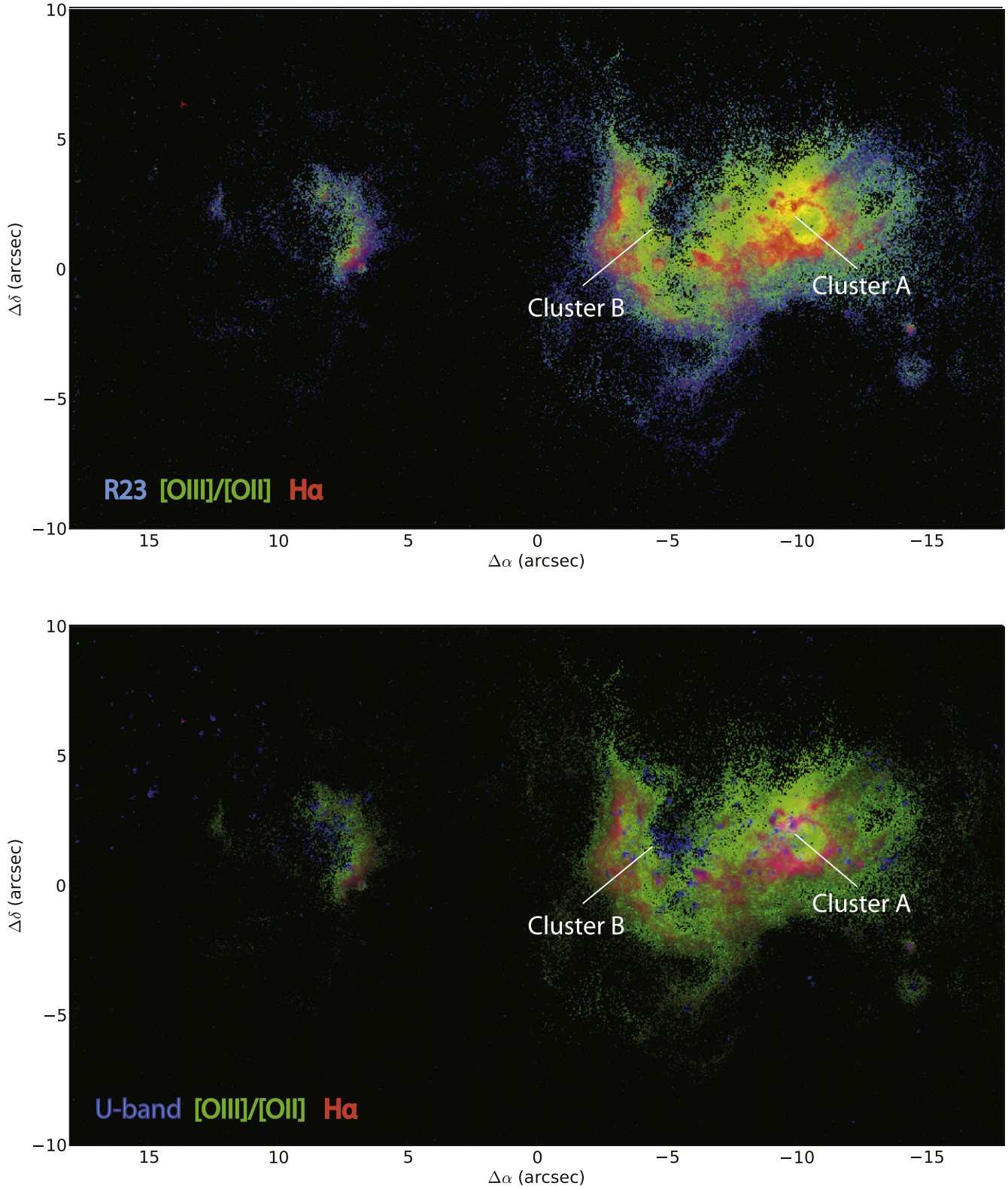

Figure 13. To illustrate the benefits of ultra-high-resolution emission-line imaging, here we create a color composite of Mrk 71 in R_{23} (i.e., metallicity, blue), [O III]/[O II] (i.e., ionization strength, green) and Hα (ionized gas, red). In the bottom panel we replace R_{23} with the U band, to highlight the position of hot, young stars. The locations of the two main clusters (A and B) within Mrk 71 are labeled in both images.

Drissen et al. (2000) estimate that the total energy returned to the ISM via winds from the stars in the core of cluster B, over 2.5 Myr since the starburst, would be 5×10^{50} erg. While this is two orders of magnitude less than the kinetic energy in the expanding superbubble surrounding Mrk 71 (Roy et al. 1991, 1992), the stars within the core of cluster B may be capable of creating the small cavity in the surrounding ISM that we see here.

5. DISCUSSION

The observations presented here provide insight into a local star-forming galaxy on 2 pc scales. What do we gain from observing star-forming galaxies on such fine spatial scales? The first and perhaps most obvious gain is that we can observe complex structure in the ionizing gas, with respect to both the morphology of the gas and the physical feedback effects of stars (bubbles, blowout, etc.). For example, we have seen that a cluster of three WR stars may be capable of blowing out a region ∼18–28 pc in size. Using the morphology of emission lines, we can investigate the presence of thin filamentary fronts (typically ∼10 pc), changes in the ionization state of the gas, and also possible chemical structure.

The fine spatial scales utilized here enable us to "image" rather than "map" the physical conditions throughout Mrk 71. To illustrate this concept, in Figure 14 we show color-composite images constructed from images of metallicity (R_{23}), ionization strength ([O III]/[O II]), ionized gas (Hα emission), and hot, young stars (U-band image). Each color channel uses the original (0.″04 pixel^{-1}) narrowband images and is not masked with respect to the signal in each pixel. Despite the lack of quantitative value, these images can be used to investigate the effects of feedback throughout Mrk 71. For example, in the top panel of Figure 14 the Hα emission (red) is seen to dominate along edges surrounding the highly ionized gas (green), with metallicity gradient peaking along the outer edges of the galaxy. The edge of the ionized bubble, which may have caused the ring of low-metallicity gas shown in Figure 9, is clearly apparent, and the decrease in ionization from the inside of the bubble is seen as a ring of yellow. In the bottom panel, R_{23} is replaced with the U band, which traces the continuum emission of hot, young stars. While cluster B can be seen clearly (in the "crux" of the arm), cluster A is embedded behind the Hα emission on the northeast edge of the Hα emission. Both pictures are in line with the findings of Drissen et al. (2000), who suggest that cluster A is so young (<1 Myr) that it is still embedded in dust, although a significant fraction of the UV radiation emitted by its hidden massive stars manages to leak out of the dust to provide the bulk of ionizing flux for Mrk 71. In NGC 2366-II there is a scattering of stars along the eastern edge—most likely the cause of the ionized gas front and [S II]/Hα and [O III]/Hβ gradients seen in Figures 6 and 7.

Despite the large amounts of energy being injected into the ISM throughout Mrk 71, our emission-line diagnostic images clearly show that the gas is predominantly photoionized. However, the lack of detectable shock excitation remains puzzling given the young, intense star formation and consequently outflowing gas. This nondetection may in part be due to the fact that our observations lack kinematical information. If we had instead observed Mrk 71 with a high spatial resolution IFU, we would undoubtably see emission lines with multiple velocity components along the line of sight, thereby providing a far more complete and accurate view of the ISM. For example, gas moving at different velocities along the line of sight would give a range of line centroids and gas at different temperatures would produce profiles with different line widths (owing to line broadening). Of course, we would still be unable to disentangle velocity components perpendicular to the line of sight, so a favorable geometry would also be beneficial here. Nevertheless, using individual line kinematics, one could decompose the emission-line components to obtain separate and more accurate line ratios, a technique commonly used in IFU studies (James et al. 2009, 2013a, 2013b; Amorín et al. 2012; Hägele et al. 2012; Westmoquette et al. 2013). As demonstrated by Rich et al. (2011, 2014), this method can be especially effective in isolating shock-excited emission, which may at present be lost among the more dominant emission-line components from photoionization.

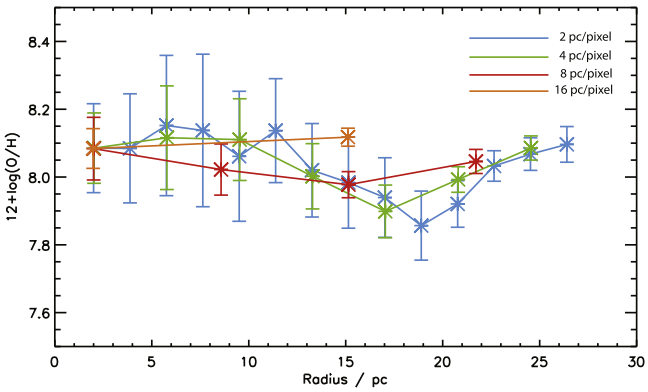

Figure 14. Effects of decreasing spatial resolution. Here we show the radial gradient originally shown in Figure 9(b) at 2 pc pixel^{-1} resolution, degraded to 4, 8, and 16 pc pixel^{-1} resolution.

We find the He II emission from cluster A rather intriguing, given the extreme youth of the cluster ($\lesssim$1 Myr). Its age dictates that the emission cannot be due to WR stars, and despite the fact that the He II/Hβ flux ratio from cluster A can be reconciled via photoionization models, it is only done so by assuming input spectra from planetary nebula nuclei, - which would also exist long after the cluster's age. One way to achieve nebular He II emission in a young stellar system would be from the hard ionizing flux from very massive stars (Crowther et al. 2010). Such stars, which can be as massive as 300 $M_{\odot}$, may be present within young clusters and would have powerful stellar winds and a significantly increased ionizing flux compared to lower-mass stars. As such, both broad and narrow He II emission features would be present and reminiscent of WR populations, despite the clusters being at an early evolutionary phase (1–2 Myr; Crowther et al. 2010). The existence of very massive stars has also been proposed in NGC 5253 by Calzetti et al. (2015) to explain the ionizing flux from the extremely young clusters ($\lesssim$1 Myr) located within the "radio nebula," where nitrogen-rich WR stars have also been detected.

The detailed chemical structure observed in Mrk 71 (which we discuss in Section 4.2) would of course be lost if we instead imaged Mrk 71 on larger spatial scales. This is illustrated in Figure 13, where we show the radial gradient originally shown in Figure 9(b) at 2 pc pixel^{-1} resolution, degraded to 4, 8, and 16 pc pixel^{-1} resolution, and the gradient is seen to diminish almost entirely at 8 pc pixel^{-1}. While unsurprising, this loss in structure with resolution does highlight the need for care when assessing metallicity gradients and their evolution across cosmic time. As shown by Yuan et al. (2013), for each individual metallicity gradient there is a critical angular resolution FWHM below which the measured metallicity gradient is flattened. This has a significant consequence when interpreting the apparent steepening of metallicity gradients with redshift, especially when the highest-redshift observations are aided by gravitational lensing and adaptive optics. However, it should be noted that the spatial resolution does *not* affect the calculation of the galaxy's average metallicity—from all pixels within Figure 9 we calculate a mean of 12 + log

$(O/H) = 8.04 \pm 0.11$, and if we use the total, reddening-corrected fluxes from the [O III], [O II], and Hβ images and the lower-branch R_{23} diagnostic, we derive $12 + \log(O/H) = 8.02 \pm 0.15$. This effect was first demonstrated by Kobulnicky & Skillman (1998) and more recently by Mast et al. (2014), where IFU observations of spiral galaxies at ~45 pc arcsec^{-1}are simulated up to 1 kpc arcsec^{-1} to show that any smooth, global trends remain observable at larger spatial scales but any sharp structure is lost. These results provide hope for the use of metallicity diagnostics on high-z galaxies where spatially resolved line ratios are not available and we are required to integrate light over the entire galaxy.

While the data presented here clearly illustrate the gains from high spatial resolution observations, they also demonstrate the need for care when working with emission-line diagnostics on such scales. As discussed previously in Section 4.2, emission-line-based metallicity calibrations have been designed to provide us with information integrated over entire H II regions rather than *throughout* H II regions. In addition to this, emission-line diagnostics were derived from photoionization models and, at 2 pc scales, excitation due to photoionization may not dominate. Both of these points need to be taken into consideration as we enter the era of extremely large telescopes. At the end of the next decade, observing gas structure on such small scales will not only be limited to the local universe with both ground- and space-based observatories, with telescopes such as the E-ELT, GMT, and TMT being designed to probe <50 pc scales out to redshifts as high as $z = 2$. Despite engaging with the fine-scale ISM structure that we have presented here, we may still need to integrate over >20 pc regions if we intend to continue using strong-line ratio diagnostics.

6. CONCLUSIONS

This paper presents an extensive data set of new *HST*-WFC3 observations of Mrk 71, one component of a nearby ($D \sim 3.44$ Mpc) BCD galaxy containing one of the most powerful local starbursts known. The data consist of high-resolution (0.″04 pixel^{-1}) images in seven narrowband and four broadband filters, enabling us to create continuum-subtracted images of Mrk 71 in the light of [O II] ($\lambda3727 + \lambda3729$), He II $\lambda4686$, Hβ, [O III] $\lambda5007$, Hα, and [S II] ($\lambda6716 + \lambda6731$). The final binned data provide emission-line images for all lines at spatial resolutions of ~2 pc pixel^{-1} at 3σ confidence levels, with the exception of He II, which we use at the 1σ confidence level. NGC 2366-II is also seen within our data, although it is not the primary focus of our work.

The data presented here complement a plethora of multi-wavelength observations of Mrk 71, which have been documented extensively in the literature. From these studies, we know Mrk 71 to be a low-metallicity (~0.17 $Z_\odot$) giant H II region in NGC 2366 that consists of two main stellar clusters, A and B (Figure 1). It is known to harbor an expanding superbubble that envelopes the entire system and a chimney of outflowing gas extending north–northwest away from the superbubble. Mrk 71 is perhaps most famous for displaying signs of hypersonic gas (lines with FWHM ~ 2400 km s^{-1}) around cluster A.

Using the high-resolution emission-line images, we explore the chemical and physical properties of the ionized gas throughout Mrk 71 in unprecedented detail and deduce the following:

1. Each emission-line image shows one clear peak in flux surrounding cluster A, a super star cluster, whereas cluster B is located in a cavity of emission with an arm of ionized gas extending northward along its eastern edge. The morphology of the ionized gas is less extended in the lower-ionization lines, [S II] and [O II], than in the [O III] and Balmer line images. Both the [S II] and [O II] images show a pronounced shell of emission around cluster A, which we interpret as the edges of an ionized gas bubble ~22 pc in diameter or a single H II region.
2. The [O III]/Hβ and [S II]/Hα line ratio images show an extensive amount of structure, with a strong peak in [O III]/Hβ surrounding cluster A and a distinct gradient in both ratios as you move away from cluster A and along the edges of cluster B and NGC 2366-II. Putting both ratios onto an emission-line diagnostic plot on a pixel-by-pixel basis, we find the gas to be predominantly photoionized throughout, with no sign of shock excitation. We confirm the findings of Drissen et al. (2000), who suggest that cluster A is responsible for the bulk of ionizing photons for the galaxy, although our line ratio images suggest evidence for a non-negligible contribution from cluster B also. Photoionization models reveal the gas to be of high density, with $\log(U) = -1$ to -2, between 0.15 and 0.2 $Z_\odot$, and a range of opacities.
3. Using the [O III], [O II], and Hβ images and the strong-line metallicity diagnostic, R_{23}, we create the first "metallicity image" of a galaxy, i.e., on spatial scales of 2 pc. The image reveals that the gas within Mrk 71 is not chemically homogeneous, with chemical structure on scales larger than the 1σ distribution of metallicity throughout the system. There is an increase in metallicity outward from cluster B and across the eastern arm (~45 pc in width). Moreover, a ring-shaped decrease in metallicity is seen surrounding cluster A, ~26 pc across with an edge ~5–10 pc thick, which aligns with the shell of [O II] and [S II] emission discussed above. We attribute this structure to the fact that we are spatially resolving gas across a Strömgren sphere rather than integrating over it, and here the R_{23} diagnostic, which was designed to work over entire H II regions, breaks down.
4. The He II image, which traces both the 4650 Å WR feature and the nebular He II $\lambda4686$ emission, reveals five strong peaks in emission, one in cluster A and four in cluster B. Upon inspection of the unbinned He II image (i.e., at 0.″04 pixel^{-1}), the peaks were resolved into individual WR stars, with the strongest peak in cluster B showing a cluster of three WR stars. However, at the 3σ level, only the strongest peaks in clusters A and B are detected. Considering the young age of cluster A and its high density of ionizing photons, we conclude that the He II emission within this cluster is either purely nebular in origin or due to very massive stars. We therefore detect a total of three WR stars in Mrk 71 (each located in cluster B, although three more may potentially be present).
5. A small blowout cavity is detected at the edge of the WR cluster in cluster B, which is ~18 pc across in [O III] and Hβ and ~28 pc across in [O II] emission. The cavities align well with the direction of extended nebular He II

emission seen by Drissen et al. (2000) and the "chimney" of outflowing gas (Roy et al. 1991). We suspect that the energy ejected into the ISM from this WR cluster, combined with that from dozens of massive OB stars seen in the vicinity, may be responsible for blowing out the ionized gas surrounding cluster B and creating this emission-line cavity.

6. We demonstrate that emission-line images of this kind can be used in their ratioed form to create "feedback images," i.e., color composites that show the physical conditions of the gas, such as the strength of the ionizing radiation ([O III]/O II) or metallicity (R_{23}), along with the ionizing sources themselves. Such images can be used to investigate the effects of feedback throughout star-forming systems. For Mrk 71, these images highlight the structure of the ionized gas in relation to the ionizing sources, the extent of the H II region surrounding cluster A, and the ionization gradient along its edge.

The observations presented here offer an insight into the ultra-high spatial resolution observations achievable from both current and future ground-based AO-assisted IFU instruments. High spatial resolution emission-line images have enabled us to explore the chemical and physical structure of the ISM on a parsec-by-parsec basis throughout a low-metallicity star-forming galaxy—a local analog to young galaxies in the high-z universe. By observing galaxies of this kind on such fine spatial scales, we can observe the full complexity of the ionized gas, with regard to both its morphology and ionization state and also the physical effects of the stellar feedback (e.g., outflows/superwinds) in primordial-like systems. In Mrk 71, the energy injected into the ISM from the winds of massive stars has succeeded in blowing out a large cavity of ionized gas, possibly contributing to a large-scale outflow of gas away from the main body. Regulating mechanisms such as this are thought to suppress star formation and prevent low-mass halos from forming dwarf galaxies. On the other hand, stellar superwinds are providing an efficient mechanism for transporting photons and material outside of the dwarf galaxy, suggesting that small systems of this kind may play a role in the reionization of the universe at $z = 6$–11.

Our metallicity images enable us to observe chemical inhomogeneity on <50 pc scales and (apparent) changes in chemical structure across Mrk 71 on scales as small as 2 pc pixel^{-1}. Although the structure is lost at degraded resolutions, it does not affect the average measured metallicity of the galaxy, offering hope for the use of metallicity diagnostics on high-z galaxies where light is integrated over large spatial scales.

While the gains of high-resolution emission-line images are obvious, we have also shown that the use of strong-line diagnostics may not be possible in this regime. For example, metallicity diagnostics were designed and calibrated on emission-line ratios integrated over entire H II regions, and using them on spatially resolved emission across an H II region may cause erroneous or misleading results. Such limitations on our much-loved strong-line methods are especially important as we enter the era of 30–40 m telescopes and start probing <50 pc scales at $z = 2$.

Finally, we note that the data presented here are inherently flawed in comparison to the future high spatial resolution ($<0\farcs2$) IFU spectroscopic observations, which will allow us to access the third dimension of our emission-line maps—velocity. High-resolution velocity maps of the outflowing gas from cluster B and the ionized bubble surrounding cluster A would enable us to explore the full complexity of feedback effects, e.g., by mapping expansion velocities and mass-loading factors for the gas entrained in each structure, and uncovering shock excitation from separated emission-line components.

Observations such as those presented here provide excellent benchmarks for the high spatial resolution hydrodynamical simulations that endeavor to model a "realistic" ISM, with an aim to understanding the triggering and evolution of star formation in galaxies throughout the universe.

The authors give thanks to Roberto Maiolino, Max Pettini, and Francesco Belfiore for invaluable discussions concerning the content of this paper, and to Rob Kennicutt for his insightful comments on this manuscript. We also greatly appreciated discussions and assistance from Mike Dopita and Ralph Sutherland regarding photoionization modeling with MAPPINGS. We would like to sincerely thank Sungryong Hong for assisting us in the testing of continuum-subtraction methods and Jay Anderson for help with WFC3 image reduction. We sincerely thank the reviewer of the paper, whose helpful comments and suggestions greatly improved the paper. STScI is operated by the Association of Universities for Research in Astronomy, Inc., under NASA contract NAS5-26555. Support for Program number 13041 was provided by NASA through a grant from the Space Telescope Science Institute, which is operated by the Association of Universities for Research in Astronomy, Incorporated, under NASA contract NAS5-26555.

Facility: *HST* (WFC3).

REFERENCES

Allen, M. G., Groves, B. A., Dopita, M. A., Sutherland, R. S., & Kewley, L. J. 2008, ApJS, 178, 20
Amorín, R., Vílchez, J. M., Hägele, G. F., et al. 2012, ApJL, 754, L22
Asplund, M., Grevesse, N., Sauval, A. J., & Scott, P. 2009, ARA&A, 47, 481
Baldwin, J. A., Phillips, M. M., & Terlevich, R. 1981, PASP, 93, 5
Belfiore, F., Maiolino, R., Bundy, K., et al. 2015, MNRAS, 449, 867
Binette, L., Drissen, L., Ubeda, L., et al. 2009, A&A, 500, 817
Bovill, M. S., & Ricotti, M. 2009, ApJ, 693, 1859
Braun, R. 1995, A&AS, 114, 409
Bruzual, G., & Charlot, S. 2003, MNRAS, 344, 1000
Bryant, J. J., Owers, M. S., Robotham, A. S. G., et al. 2015, MNRAS, 447, 2857
Bundy, K., Bershady, M. A., Law, D. R., et al. 2015, ApJ, 798, 7
Calzetti, D., Conselice, C. J., Gallagher, J. S., III, & Kinney, A. L. 1999, AJ, 118, 797
Calzetti, D., Harris, J., Gallagher, J. S., III, et al. 2004, AJ, 127, 1405
Calzetti, D., Johnson, K. E., Adamo, A., et al. 2015, ApJ, 811, 75
Campbell, A., Terlevich, R., & Melnick, J. 1986, MNRAS, 223, 811
Cappellari, M., Emsellem, E., Krajnovíc, D., et al. 2011, MNRAS, 413, 813
Cresci, G., Mannucci, F., Maiolino, R., et al. 2010, Natur, 467, 811
Crowther, P. A. 2007, ARA&A, 45, 177
Crowther, P. A., Schnurr, O., Hirschi, R., et al. 2010, MNRAS, 408, 731
De Young, D. S., & Heckman, T. M. 1994, ApJ, 431, 598
Dopita, M. A., Sutherland, R. S., Nicholls, D. C., Kewley, L. J., & Vogt, F. P. A. 2013, ApJS, 208, 10
Drissen, L., Roy, J.-R., & Robert, C. 1997, ApJL, 474, L35
Drissen, L., Roy, J.-R., Robert, C., Devost, D., & Doyon, R. 2000, AJ, 119, 688
Elmegreen, B. G., & Lada, C. J. 1977, ApJ, 214, 725
Ferrara, A., & Tolstoy, E. 2000, MNRAS, 313, 291
Fitzpatrick, E. L. 1999, PASP, 111, 63
Gonzalez-Delgado, R. M., Perez, E., Tenorio-Tagle, G., et al. 1994, ApJ, 437, 239
Guo, Q., White, S., Li, C., & Boylan-Kolchin, M. 2010, MNRAS, 404, 1111
Guseva, N. G., Izotov, Y. I., & Thuan, T. X. 2000, ApJ, 531, 776

Hägele, G. F., Firpo, V., Bosch, G., Díaz, Á. I., & Morrell, N. 2012, MNRAS, 422, 3475
Heckman, T. M., González-Delgado, R., Leitherer, C., et al. 1997, ApJ, 482, 114
Hong, S., Calzetti, D., & Dickinson, M. 2014, PASP, 126, 79
Hong, S., Calzetti, D., Dopita, M. A., et al. 2011, ApJ, 731, 45
Hunter, D. A., Ficut-Vicas, D., Ashley, T., et al. 2012, AJ, 144, 134
Izotov, Y. I., Lipovetsky, V. A., Chaffee, F. H., et al. 1997, ApJ, 476, 698
Izotov, Y. I., & Thuan, T. X. 2011, ApJ, 734, 82
Izotov, Y. I., Thuan, T. X., & Guseva, N. G. 2007, ApJ, 671, 1297
James, B. L., Tsamis, Y. G., & Barlow, M. J. 2010, MNRAS, 401, 759
James, B. L., Tsamis, Y. G., Barlow, M. J., Walsh, J. R., & Westmoquette, M. S. 2013a, MNRAS, 428, 86
James, B. L., Tsamis, Y. G., Barlow, M. J., et al. 2009, MNRAS, 398, 2
James, B. L., Tsamis, Y. G., Walsh, J. R., Barlow, M. J., & Westmoquette, M. S. 2013b, MNRAS, 430, 2097
Kehrig, C., Pérez-Montero, E., Vílchez, J. M., et al. 2013, MNRAS, 432, 2731
Kehrig, C., Vílchez, J. M., Pérez-Montero, E., et al. 2015, ApJL, 801, L28
Kehrig, C., Vílchez, J. M., Sánchez, S. F., et al. 2008, A&A, 477, 813
Kennicutt, R., Balick, B., & Heckman, T. 1980, PASP, 92, 134
Kennicutt, R. C., Jr. 1989, ApJ, 344, 685
Kennicutt, R. C., Jr., & Skillman, E. D. 2001, AJ, 121, 1461
Kewley, L. J., & Dopita, M. A. 2002, ApJS, 142, 35
Kewley, L. J., Dopita, M. A., Sutherland, R. S., Heisler, C. A., & Trevena, J. 2001, ApJ, 556, 121
Klypin, A., Kravtsov, A. V., Valenzuela, O., & Prada, F. 1999, ApJ, 522, 82
Kobulnicky, H. A., Kennicutt, R. C., Jr., & Pizagno, J. L. 1999, ApJ, 514, 544
Kobulnicky, H. A., & Skillman, E. D. 1996, ApJ, 471, 211
Kobulnicky, H. A., & Skillman, E. D. 1997, ApJ, 489, 636
Kobulnicky, H. A., & Skillman, E. D. 1998, ApJ, 497, 601
Kunth, D., & Östlin, G. 2000, A&ARv, 10, 1
Leitherer, C., Schaerer, D., Goldader, J. D., et al. 1999, ApJS, 123, 3
López-Sánchez, Á R., Esteban, C., García-Rojas, J., Peimbert, M., & Rodríguez, M. 2007, ApJ, 656, 168
López-Sánchez, Á R., Mesa-Delgado, A., López-Martín, L., & Esteban, C. 2011, MNRAS, 411, 2076
Mac Low, M.-M., & Ferrara, A. 1999, ApJ, 513, 142
Marconi, G., Matteucci, F., & Tosi, M. 1994, MNRAS, 270, 35
Martin, C. L. 1998, ApJ, 506, 222
Mast, D., Rosales-Ortega, F. F., Sánchez, S. F., et al. 2014, A&A, 561, A129
McCray, R., & Kafatos, M. 1987, ApJ, 317, 190
McGaugh, S. S. 1991, ApJ, 380, 140
Monreal-Ibero, A., Walsh, J. R., & Vílchez, J. M. 2012, A&A, 544, A60
Moustakas, J., & Kennicutt, R. C., Jr. 2006, ApJS, 164, 81
Müller Sánchez, F., Davies, R. I., Eisenhauer, F., et al. 2006, A&A, 454, 481
Noeske, K. G., Guseva, N. G., Fricke, K. J., et al. 2000, A&A, 361, 33
Pagel, B. E. J., Edmunds, M. G., Blackwell, D. E., Chun, M. S., & Smith, G. 1979, MNRAS, 189, 95
Pérez, E., González Delgado, R., & Vílchez, J. M. 2001, ApSSS, 277, 83
Pérez-Montero, E., Vílchez, J. M., Cedrés, B., et al. 2011, A&A, 532, A141
Perret, V., Renaud, F., Epinat, B., et al. 2014, A&A, 562, A1
Pettini, M., & Pagel, B. E. J. 2004, MNRAS, 348, L59
Queyrel, J., Contini, T., Kissler-Patig, M., et al. 2012, A&A, 539, A93
Rauch, T. 2003, A&A, 403, 709
Renaud, F., Bournaud, F., Kraljic, K., & Duc, P.-A. 2014, MNRAS, 442, L33
Rich, J. A., Kewley, L. J., & Dopita, M. A. 2011, ApJ, 734, 87
Rich, J. A., Kewley, L. J., & Dopita, M. A. 2014, ApJL, 781, L12
Roy, J.-R., Aube, M., McCall, M. L., & Dufour, R. J. 1992, ApJ, 386, 498
Roy, J.-R., Belley, J., Dutil, Y., & Martin, P. 1996, ApJ, 460, 284
Roy, J.-R., Boulesteix, J., Joncas, G., & Grundseth, B. 1991, ApJ, 367, 141
Sánchez Almeida, J., Morales-Luis, A. B., Muñoz-Tuñón, C., et al. 2014, ApJ, 783, 45
Searle, L., & Sargent, W. L. W. 1972, ApJ, 173, 25
Teyssier, R., Chapon, D., & Bournaud, F. 2010, ApJL, 720, L149
Thuan, T. X., Bauer, F. E., & Izotov, Y. I. 2014, MNRAS, 441, 1841
Thuan, T. X., & Izotov, Y. I. 2005, ApJS, 161, 240
Tolstoy, E., Saha, A., Hoessel, J. G., & McQuade, K. 1995, AJ, 110, 1640
Walsh, J. R., & Roy, J.-R. 1989, MNRAS, 239, 297
Westmoquette, M. S., James, B., Monreal-Ibero, A., & Walsh, J. R. 2013, A&A, 550, A88
Westmoquette, M. S., Smith, L. J., Gallagher, J. S., & Exter, K. M. 2007, MNRAS, 381, 913
Yuan, T.-T., Kewley, L. J., & Rich, J. 2013, ApJ, 767, 106